INCLUSIVE PUBLISHING
TRUSTED SCIENCE

TOPICAL REVIEW • OPEN ACCESS

Nanocomposite materials as observed by mass-selective neutron spectroscopy

To cite this article: Matthew Krzystyniak *et al* 2024 *J. Phys. Commun.* **8** 022001

View the article online for updates and enhancements.

You may also like

Journal of Physics Communications

TOPICAL REVIEW

Nanocomposite materials as observed by mass-selective neutron spectroscopy

Matthew Krzystyniak[1,*] , Giovanni Romanelli[2], Beata Grabowska[3] and Felix Fernandez-Alonso[4,5,6,7]

1   ISIS Neutron and Muon Source, STFC Rutherford Appleton Laboratory, OX11 0QX, United Kingdom
2   Dipartimento di Fisica and NAST Centre, Università degli Studi di Roma Tor Vergata, 00133. Roma, Italy
3   AGH University of Science and Technology, Faculty of Foundry Engineering, Reymonta 23, 30–059 Krakow, Poland
4   Materials Physics Centre, CSICUPV/EHU, 20018 Donostia-San Sebastian, Spain
5   Donostia International Physics Center (DIPC), 20018 Donostia-San Sebastian, Spain
6   Department of Physics and Astronomy, University College London, Gower Street, London WC1E 6BT, United Kingdom
7   IKERBASQUE, Basque Foundation for Science, 48009 Bilbao, Spain
*   Author to whom any correspondence should be addressed.

E-mail: matthew.krzystyniak@stfc.ac.uk

Abstract

This work provides a current, critical view of the application of MAss-selective Neutron SpEctroscopy (MANSE) to nanocomposite materials. MANSE is a unique technique made possible owing to the existence of the pulsed neutron sources. At present, the only operating MANSE spectrometer in the world, VESUVIO, is located at the ISIS Neutron and Muon Source in the UK. We start by providing a brief description of the neutron Compton scattering, the anatomy of a mass-selective neutron spectrometer, and the experimental data treatment. We continue by briefly outlining the main quantum mechanical concepts, models and approximations relevant both to the *ab initio* prediction and experimental measurement of main MANSE observables. Next, we present several recent exemplars chosen to highlight the use of MANSE in the field of nanocomposites. Our examples include, in chronological order, encapsulated nanoparticles in amorphous silica gel, bioactive glass-ionomer cement, Cu-Ti-C composites, and sodium carboxymethyl starch-based binders in the presence of a mineral matrix. We close by providing our view of the ongoing and future challenges and opportunities in the mass-selective neutron investigation of NQEs in nanocomposite materials.

1. A brief introduction

The technique of neutron Compton scattering (NCS), also referred to as deep-inelastic neutron scattering (DINS), was first reviewed almost twenty years ago [1], following a series of reviews published a decade later [2–4]. During this time, NCS has witnessed an unprecedented upsurge of experimental activity that was linked to a flurry of theoretical and computational work, both paving the way for the technique to join the mainstream developments in spectroscopic studies of condensed matter systems. These efforts were driven by the need to understand and exploit the properties of advanced, functional materials.

Composite materials have added new dimensions to the design and construction of modern infrastructure and thus have been introduced into almost every industry in some shape or form. The NCS technique is very well suited for the investigation of the dynamical properties of composite materials owing to its inherent ability to investigate the nuclear quantum dynamics in condensed matter systems in a mass-resolved manner. It is this specific feature of the NCS technique as applied to the investigation of functional materials that has largely contributed to coining the term 'Mass-Selective Neutron Spectroscopy' (MANSE).

In this review, we summarise recent efforts to include the composite materials in the portfolio of condensed matter systems investigated by the MANSE technique using the unique VESUVIO instrument located at the ISIS Facility, Rutherford Appleton Laboratory, UK. In section 2, we provide a brief description of the anatomy of an

NCS experiment, including the experimental data treatment. In section 3, we introduce nuclear quantum effects, which are the source of NCS observables, and in section 3.5, we describe how these observables are linked to the NCS technique via measurement. In section 4, we present several recent examples of the application of MANSE in the field of nanocomposites, including encapsulated nanoparticles in amorphous silica gel, bioactive glass-ionomer cement, Cu-Ti-C composites, and sodium carboxymethyl starch-based binders in the presence of a mineral matrix. We close in section 5 by providing our view of the ongoing and future challenges and opportunities in the mass-selective neutron investigation of NQEs in nanocomposite materials.

2. Mass-Selective Neutron Spectroscopy

2.1. Neutron Compton scattering

Detailed descriptions of the VESUVIO spectrometer have been provided by the previous review articles and book chapters [1–6], and the reader is referred to these references for an in-depth understanding of the inner workings of this unique neutron beam line as well as the anatomy of measurements. Here, we will focus on a description adopting more of an experimentalist's view, highlighting the unique aspects of the MANSE technique as implemented on VESUVIO and its experimental data treatment.

Composite materials often consist of many different local microscopic environments. As the MANSE technique does not use pixelated neutron detectors and the signals are gathered from the entire volumes of macroscopic samples, typically covering the entire cross-sectional area of the incident neutron beam of the order of 25 cm^2 [7], only an average neutron response function is observable. Thus, in what follows, we will concentrate on the description of the neutron observables, which do not depend on the direction but rather on the magnitude of the neutron momentum transfer. We will write vectors in bold letters and their moduli and other scalar variables in normal font letters. Moreover, in our description, we will use the system of units typically adopted for the neutron Compton scattering technique. Hereinafter, momentum transfer will be given in units of Å^{-1}, energy transfer ω in meV, mass in atomic mass units (amu). With this choice of units, the value of the reduced Plank constant is 2.044 58 [(meV amu)$^{1/2}$Å] [8].

Vesuvio is a so-called inverted-geometry time-of-flight (TOF) neutron spectrometer [1–6], meaning that a sample mounted on Vesuvio views a white (broad energy) incoming neutron beam, and the final energy of the neutrons scattered from the sample, E_1, is measured (fixed) by a final neutron energy analyser, which—in the case of epithermal neutrons—is a thin foil made out of material strongly (and resonantly) absorbing neutrons in a narrow energy band in the electron-volt energy range. Additionally, the TOF technique is employed in order to measure the time of fight of neutrons, t, spanning the time between the moment they leave the neutron water moderator, are scattered by the sample, and finally, get absorbed by the neutron energy analyser. In this way, the magnitudes of the incident neutron velocity, v_0, momentum, $k_0 = \frac{m v_0}{\hbar}$, and the incident neutron energy $E_0 = \frac{\hbar^2 k_0^2}{2m}$ (with m being the neutron mass and $\hbar$ the reduced Planck constant), are encoded in the TOF domain in the form of the following equation:

$$t = \frac{L_0}{v_0} + \frac{L_1}{v_1} + t_0 \tag{1}$$

where L_0 is the distance from the moderator to the sample and L_1 is the distance from the sample to the detector being situated at angle θ with respect to the axis of the incident beam. v_0 and v_1 are the magnitudes (moduli) of the neutron velocities before and after the scattering process, respectively. t_0 is a time constant that determines which channel in the TOF spectrum corresponds to (infinitely fast) neutrons. This is determined by electronic delay times in the detector-discriminator-electronics-computer chain.

The entire setup of the instrument, including the choice of the inverted geometry and positioning of the detectors, is dictated by the kinematics of the Compton scattering process illustrated in figure 1.

The scattering takes place with the conservation of energy and momentum of the system consisting of the incident neutron of mass m and the target nucleus of mass M that is locally bound to its neighbouring atoms of masses M', and the bonding is mathematically represented by a potential $V(r)$. We can imagine that the nucleus of mass M is initially not at rest, but it has a non-zero value of the magnitude of the initial momentum, $\mathbf{p}_0$. Let us denote the initial and final momentum of the neutron as $\mathbf{k}_0$ and $\mathbf{k}_1$, respectively, and the associated values of the initial and final kinetic energy of the neutron as E_0 and E_1, respectively. Let us define the energy transfer of the neutron to the target nucleus, $\omega = E_0 - E_1$. We can write, $\omega = \frac{\hbar^2}{2m}(k_0^2 - k_1^2)$. We can also define the associated momentum transfer, $\mathbf{q} = \mathbf{k}_0 - \mathbf{k}_1$ with the associated magnitude, $q = (k_0^2 + k_1^2 - 2k_0 k_1 \cos\theta)^{1/2}$ and the scattering angle θ. By virtue of the momentum conservation during the scattering process, the final momentum of the nucleus after the collision with the neutron will be, $\mathbf{p}_1 = \mathbf{p}_0 + \mathbf{q}$. We can say that the nucleus recoils after the collision with the neutron due to the momentum transfer, $\mathbf{q}$. The scattering angle is defined in a spherical coordinate system, which underlies the symmetry of the scattering process, whereby the magnitude, q, does not
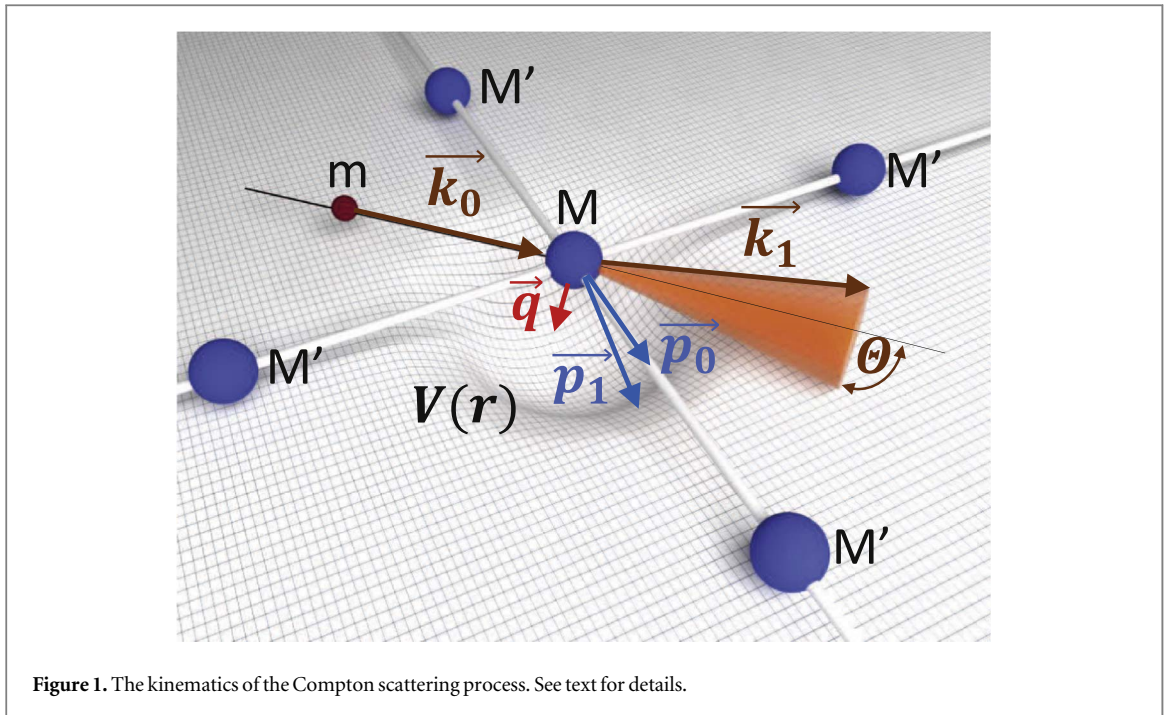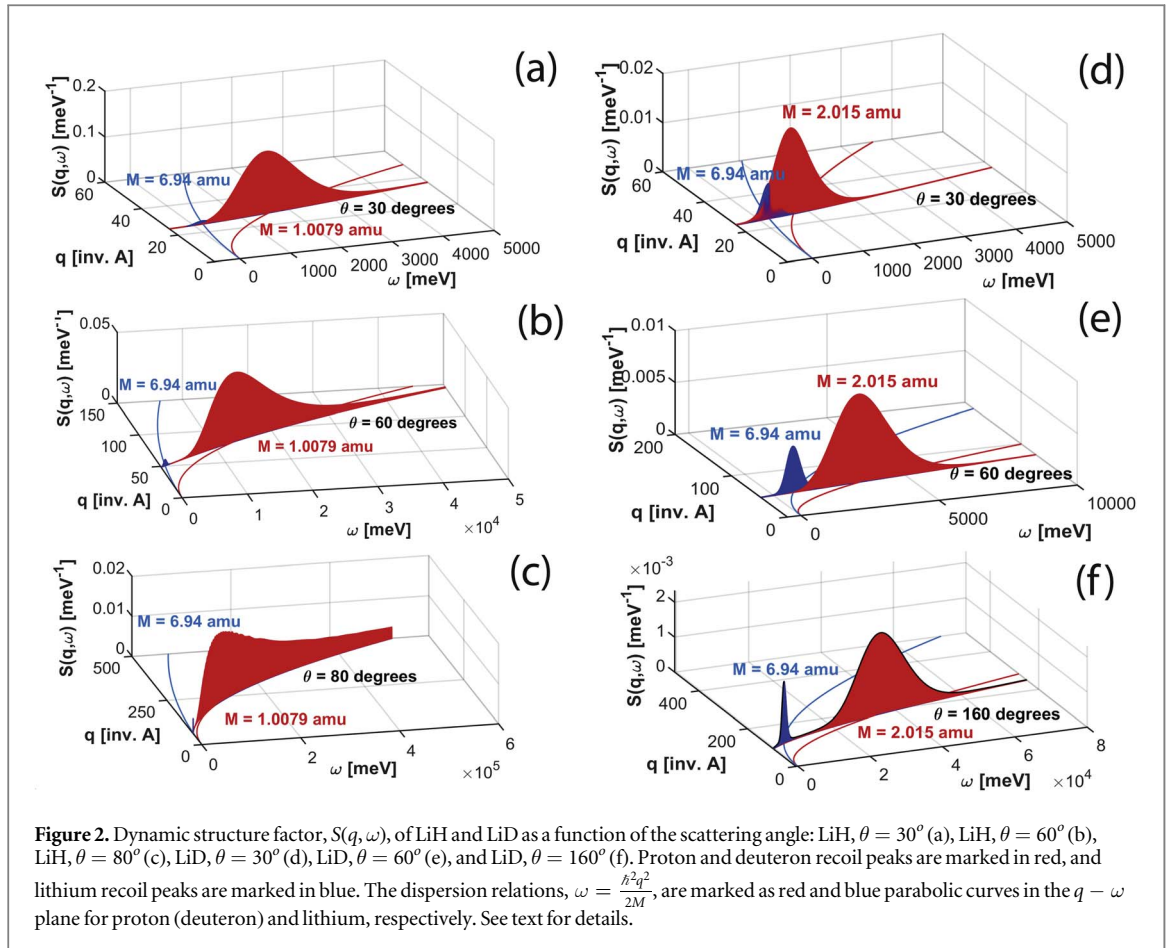
Figure 1. The kinematics of the Compton scattering process. See text for details.

depend on the azimuthal angle, ϕ. Thus, in principle, one could construct a detector bank with all detectors placed on a cone with the opening angle θ (the so-called Debye–Scherrer cone), and all detectors would detect the same information encoded in the same shapes of spectra. This is indeed planned as a future setup of the next-generation neutron Compton scattering instruments called Vesuvio plus and Etna [1–4]. In the TOF technique, for a fixed value of the final neutron energy, E_1 (and thus the fixed value of the final neutron velocity and momentum) and for a given detector placed at a fixed value of the scattering angle, θ, using equation (1), for every value of the time of flight in a recorded neutron spectrum, t, we can get discretised values of the kinematic parameters characterising the incident neutron, $E_0(t)$, $k_0(t)$, $v_0(t)$, the energy transfer, $\omega(t) = E_0(t) - E_1$, and momentum transfer, $q(t) = (k_0(t)^2 + k_1^2 - 2k_0(t)k_1 \cos \theta)^{1/2}$. From these quantities, we can build a histogrammed spectrum in the TOF domain, $C(t)$, that can be transformed into the histogrammed dynamic structure factor, $S(q(t), \omega(t))$.

   The conservation of energy and momentum during the scattering process means that, for a particular value of TOF, t_r, the energy transfer from the scattered neutrons to a given target atomic nucleus of mass M, $\omega(t_r)$, is equal to the recoil energy of the target nucleus, $\frac{\hbar^2 q(t_r)^2}{2M}$. This effective dispersion relation, $\omega = \frac{\hbar^2 q^2}{2M}$, is fulfilled for every target nucleus in the sample being measured and is at the cradle of the mass-resolved nature of the MANSE technique as implemented on Vesuvio. Namely, in order to achieve a good mass separation of the signals recorded for two target nuclei of different masses, M and M', an instrument trajectory in the $q - \omega$ plane, defined by the collection of points with loci $q(t)$, $\omega(t)$, must cross the two dispersion relations, $\frac{\hbar^2 q^2}{2M}$ and $\frac{\hbar^2 q^2}{2M'}$, at points t_r and t_r' that will be maximally separated (see figure 2 in [3], figures 5 and 6 in [2] and figure 2 below). A large degree of separation along an instrument trajectory for a given scattering angle θ is necessary because the recoil peak will occupy a single TOF bin only in the purely abstract case of a nucleus that was stationary before getting struck by an impinging neutron. Realistically, each target nucleus performs localised motion with an associated non-zero value of the kinetic energy. Importantly, this is the case even in the limit of zero temperature, where the zero-point kinetic energy is always present due to the quantum nature of the atomic nucleus. Thus, in the Compton scattering regime, we should observe in the neutron momentum transfer-energy transfer space, $q - \omega$, a recoil peak Doppler-broadened by the nuclear momentum distribution (NMD), associated with the value of the total nuclear kinetic energy of the nucleus $E_k(M)$ and centred around its value of the recoil energy $E_r = \frac{\hbar^2 q^2}{2M}$ [1]. In a TOF domain, such a Doppler-broadened recoil peak will always occupy a wide range of time bins, which can lead to an overlap with an adjacent recoil peak of a different atomic species (see figure 7 in [2]). Thus, in order to achieve good mass resolution in the MANSE technique, one has to ensure a sufficiently high momentum transfer magnitude, q, by maximising the difference between $k_0(t)$ and k_1 while keeping the scattering angle θ high. This requirement leads to the instrument design, where the difference between the initial and final energy of the scattered neutrons is maximised. The rule of thumb for the design of an NCS spectrometer states that the neutron energy transfer, $E_0(t_r) - E_1$, corresponding to the recoil peak centre at TOF value, t_r, should be much larger than the highest value of the vibrational excitation energy in the sample

Figure 2. Dynamic structure factor, $S(q,\omega)$, of LiH and LiD as a function of the scattering angle: LiH, $\theta = 30^o$ (a), LiH, $\theta = 60^o$ (b), LiH, $\theta = 80^o$ (c), LiD, $\theta = 30^o$ (d), LiD, $\theta = 60^o$ (e), and LiD, $\theta = 160^o$ (f). Proton and deuteron recoil peaks are marked in red, and lithium recoil peaks are marked in blue. The dispersion relations, $\omega = \frac{\hbar^2 q^2}{2M}$, are marked as red and blue parabolic curves in the $q - \omega$ plane for proton (deuteron) and lithium, respectively. See text for details.

under consideration [1–4]. Taking into account that the highest values of the vibrational energies observed are in the order of 0.5 eV for vibrational modes involving protons, the desired values of ω should be in the region of a few electron volts, at least in the case of neutron Compton scattering off protons.

High values of the scattering angles, necessary for the successful observation of the neutron Compton effect on a spectrometer like VESUVIO, are easily reached in backscattering, while in forward scattering, the useful range of angles needs to be optimised experimentally [1–4]. If the scattering angle, and thus the magnitude of the neutron momentum transfer, is too small, instead of smooth Doppler-broadened recoil peaks, one would rather observe a fine structure of individual vibrational or roto-vibrational lines due to neutron excitation of individual quantum transitions [1]. The fine structure will gradually disappear upon increasing the scattering angle and will adopt a smoothly broadened shape for each individual recoil peak. The limiting value of the scattering angle (or the limiting value of the momentum transfer) for which this transition occurs depends on the vibrational density of states of a given molecular or solid-state system. For example, in the case of liquid ortho-D2, this value is around 55° [1]. In practice, for many condensed matter systems, it can be as low as 30° [1–4].

In practice, the values of neutron energy transfer ω and momentum transfer q, achievable on Vesuvio, are at least an order of magnitude higher than the typical values encountered in inelastic neutron spectroscopy, and hence the DINS technique acronym. Besides the naming convention, the very high values of q are associated with an important approximation widely used in the DINS (or NCS) technique, the incoherent approximation [1–4]. Practically, the incoherent approximation means that for q values in the range of 20 to 200 Å^{-1} or higher, interference of waves representing neutrons scattered off any two neighbouring atomic species can be neglected with impunity in the neutron Compton scattering regime. In such a high-q limit, one cannot tell between the incoherent and the coherent dynamic structure factor anymore, as both dynamic structure factors merge into one entity, the total dynamic structure factor, with a multiplicative prefactor being the total (coherent plus incoherent) bound scattering cross-section. This has important experimental ramifications. Namely, in the neutron Compton scattering regime, the limit of detection (LOD) and the limit of quantitation (LOQ) of a specific atomic species is associated with its total bound neutron cross section, as all neutrons inelastically scattered by the sample 'are harvested' by the spectrometer, thus leading to a greater degree of sensitivity of the NCS technique [9]. The second important consequence of the incoherent approximation is that the total dynamic structure factor, $S(q,\omega)$, and the total count rate, $C(t)$, are algebraic sums of partial contributions (with no interference terms), $S_{i_M}(q,\omega)$, and $C_{i_M}(t)$, where i_M is an index running over different types of atomic species

in the sample under investigation, or indeed, dynamically inequivalent atomic species of the same type [1–4]:

$$C(t) = [E_0(t)I(E_0(t))]\sum_{i_M} A_{i_M} S_{i_M}(q(t), \omega(t)) = \frac{E_0(t)I(E_0(t))}{\hbar^2 q(t)}\sum_{i_M} A_{i_M} M J_{i_M}(y_{i_M}(t)) \qquad (2)$$

Experimentally, this is a very useful feature of neutron Compton scattering, as it allows for subtraction of 'unwanted' contributions, such as signals recorded by neutron detectors due to Compton scattering off sample container and other elements of the sample environment.

In equation (2), the prefactor, $[E_0(t)I(E_0(t))]$, signifies the need to normalise the experimental NCS spectrum by the initial spectrum of neutrons, $I(E_0(t))$, incident on the sample. The proportionality constant, A_{i_M}, signifies the contribution to the total count rate (the total dynamic structure factor) from the atomic species indexed i_M and is proportional to the product of the number of a given species per formula unit of the sample, N_{i_M}, and the total bound scattering cross-section of this species, $4\pi|b|^2_{i_M}$, where $|b|_{i_M}$ is the modulus of the bound scattering length of the species [1–4].

In order to convert the count rate in equation (2) into the dynamic structure factor, we can write, $S_{i_M}(q(t), \omega(t)) = \frac{M}{\hbar^2 q(t)} J_{i_M}(y_{i_M}(t))$, which holds in the so-called impulse approximation, valid for large (theoretically infinite) values of q [1–4]. Physically, this approximation implies that after an atomic nucleus has been struck by a neutron, it travels freely and that its interaction with other particles can be neglected [1]. Moreover, it is the impulse approximation that implies that scattering occurs between the neutron and a single nucleus, with the conservation of kinetic energy and momentum of the system consisting of a neutron and the nucleus [1]. The validity of the impulse approximation implies that the two dynamic variables, ω and q, can be explicitly coupled through the denition of the scaling variable y, where $y = \frac{M}{\hbar^2 q}(\omega - \frac{\hbar^2 q^2}{2M})$ [1]. This so-called 'West' or 'y-scaling' property of the neutron Compton scattering is valid for any trajectory within the neutron momentum transfer-energy transfer space, $q - \omega$. In the specific case of the instrument trajectory connecting points defined by the pairs of coordinates, $q(t), \omega(t)$, with the TOF, t, running over all time bins in a histogrammed spectrum for a constant value of the scattering angle, θ (for a given neutron detector fixed in space), we can write for a given type of atomic species:

$$y_{i_M}(t) = \frac{M}{\hbar^2 q(t)}\left(\omega(t) - \frac{\hbar^2 q(t)^2}{2M}\right) \qquad (3)$$

The West scaling variable, y, can be interpreted as the longitudinal momentum of a given nucleus defined as a projection of its radial momentum vector, $\mathbf{p}$ on the direction of the momentum transfer, $\frac{\mathbf{q}}{q}$, $y = \frac{\mathbf{p}\cdot\mathbf{q}}{q}$ [1–4]. This variable is naturally constructed in such a way that the condition $y = 0$ corresponds to the point in the $q - \omega$ space, for which, during a Compton scattering event, a stationary nucleus with mass M with initial momentum equal zero recoils freely with the recoil energy $\frac{\hbar^2 q^2}{2M}$. Anywhere outside this point, the non-zero value of y signifies that the Compton scattering has occurred for a non-stationary nucleus with some initial value of radial momentum, whose non-zero value of the projection on the direction of the momentum transfer. Two cases can be distinguished here. The energy transfer from a neutron to a struck nucleus can be less (more) than the value of the recoil energy of the initially stationary nucleus, with the corresponding negative (positive) value of y. The collection of individual neutron histories with different outcomes of the scattering process leads to a distribution of different probabilities of attaining different values of y. When histogrammed, this probability distribution will manifest as a symmetric peak in the y space of a given atomic species that will be centred around the zero value of y. The shape of this peak, referred to as the 'Compton profile', and the underlying probability distribution is termed the longitudinal momentum distribution (or nuclear momentum distribution (NMD)) and is given by the expression $J_{i_M}(y_{i_M})$ appearing in equation (2).

The most common shape of the Compton profile is an isotropic single-dimensional Gaussian [1–4]:

$$J(y) = \frac{1}{\sqrt{2\pi\sigma^2}}\exp\left(-\frac{y^2}{2\sigma^2}\right) \qquad (4)$$

where σ is the standard deviation of the momentum distribution, and the associated value of the nuclear kinetic energy, E_{kin}, can be written as $\frac{\hbar^2\sigma^2}{2M}$ in one dimension and as $\frac{3\hbar^2\sigma^2}{2M}$ in three dimensions.

The isotropic distribution signifies that the function $J(y)$ does not depend on the direction of the momentum transfer vector $\mathbf{q}$, and the only dependence is on the magnitude of this vector, q, through the definition of the y variable given by equation (3). In practice, the isotropic Gaussian Compton profile can result from a neutron Compton experiment on a system with one type of local chemical environment or from an experiment where the sample under investigation contains a collection of many different local environments whose $J(y)$ add incoherently to form a total Compton profile for a given nuclear species. Fitting an experimental shape of $J(y)$ to such a combination of profiles will most likely result in an inability to resolve individual components, and only

an average Gaussian component will be able to be fitted. Such is the case for many composite materials, in which protons form different local environments.

Experimentally, the isotropic nuclear momentum distribution that is characterised by a Gaussian function of y is never really obtained in MANSE measurements as it would require infinite magnitudes of neutron momentum transfers, q to the individual nuclear species present in the sample to fulfil the assumption underlying the impulse approximation. For finite (albeit large) amounts of q, a correction needs to be applied to account for the departures from this approximation due to the so-called 'final states effects' (FSE) [1–4]. Physically, the FSE correction is due to the fact that, after having been struck by an impinging neutron, every target nucleus in the sample recoils being subject to forces acting on it from the neighbouring nuclei. Kinematically, this results in displacements from straight-line trajectories of the recoiling nuclei. Interestingly, it is the FSE correction that introduces characteristic timescales for individual recoiling nuclei taking part in the neutron Compton scattering. Otherwise, for infinite magnitudes of q, the whole scattering process would have been instantaneous, with no time appearing anywhere in the theoretical description. These characteristic timescales, $\tau = \frac{M}{\hbar q \sigma}$, depend on the mass of the recoiling nuclei, M and the widths of their individual momentum distributions, σ [1–4]. This lets us anticipate that the FSE corrections to the nuclear momentum distributions contain information about momentum distribution widths. Indeed, with the FSE taken into account and in the case of a harmonically bound recoiling nucleus, the FSE-corrected Compton profile reads $J(y) - \frac{\sigma\sqrt{2}}{12q}\frac{d^3J(y)}{dy^3}$, where $J(y)$ is the mathematical form of the Compton profile for infinite magnitude q. Thus, in principle, one can obtain the values of σ by fitting the FSE contributions skewing the otherwise perfectly symmetrical experimental recoil peaks [5, 8, 10].

An additional difficulty in fitting neutron Compton profiles to experimental data is associated with the finite resolution of the neutron instrument in the $q - \omega$ space. Any given scattering intensity recorded by an instrument is inextricably intertwined with a finite volume in the $q - \omega$ space [11]. In other words, perfect instrument resolution would always lead to no signal being observed. Using the West-scaling property, one can associate any given resolution volume in the $q - \omega$ space with a concomitant resolution volume in the y space of a given atomic species. As mentioned above, for a sample containing multiple atomic species, the expression for the instrument count rate will contain a combination of recoil peaks, and the effect of the finite instrument resolution will be incorporated into the data analysis in the form of a convolution of each component, $J_{i_M}(y_{i_M}(t))$ with its mass-dependent resolution function, $R_{i_M}(y_{i_M}(t))$ [1–4].

With both the departures from the impulse approximation and the mass-dependent instrument resolution functions taken into account, the final MANSE fitting expression in the case of isotropic and harmonic underlying interatomic potentials takes the form:
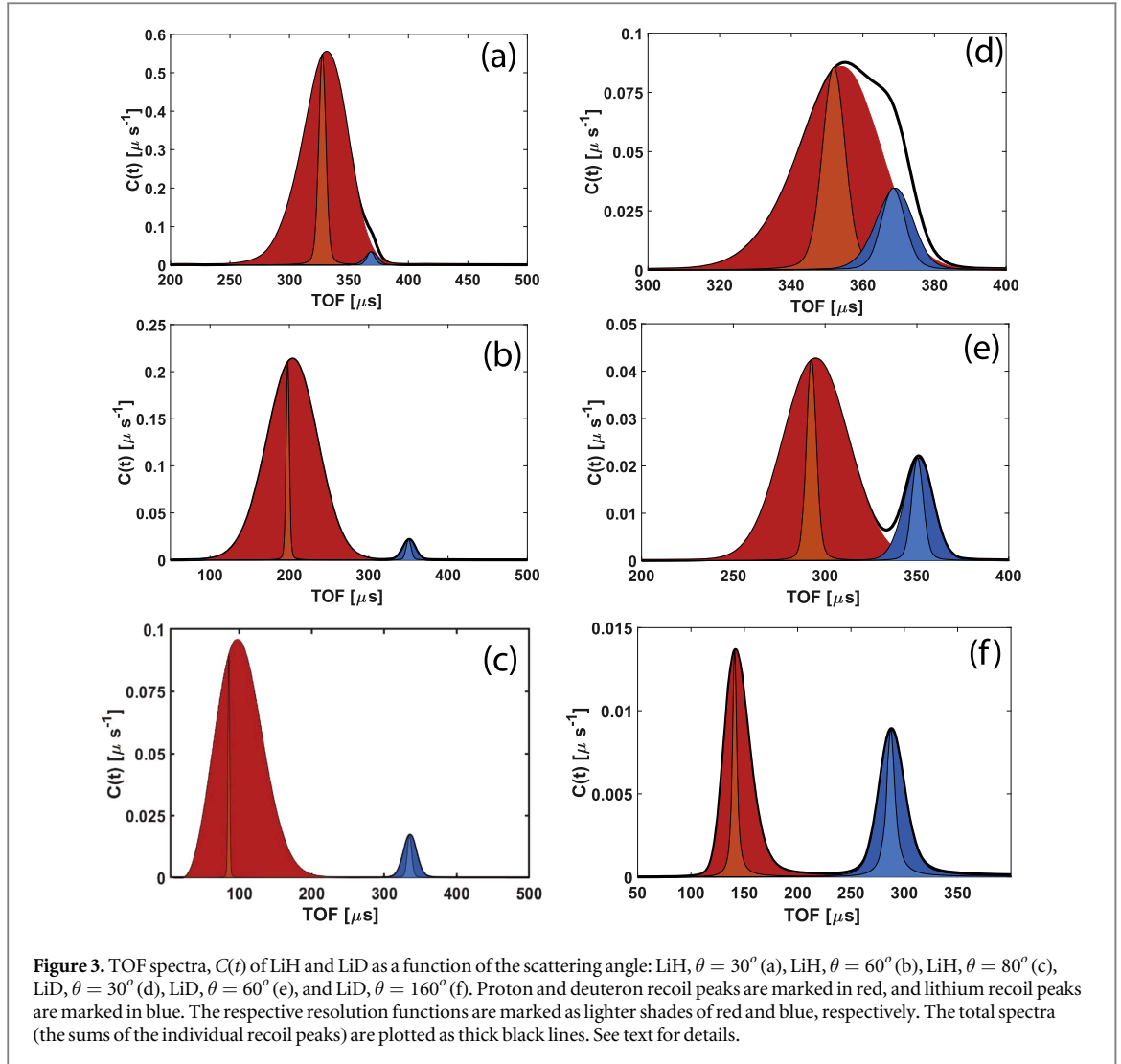
$$C(t) = \frac{E_0(t)I(E_0(t))}{\hbar^2 q(t)} \sum_{i_M} A_{i_M} M \left(J_{i_M}(y_{i_M}(t)) - \frac{\sigma\sqrt{2}}{12q(t)}\frac{d^3 J_{i_M}(y_{i_M}(t))}{dy_{i_M}(t)^3} \right) \otimes R_{i_M}(y_{i_M}(t)) \qquad (5)$$

In practice, for the current setup of the Vesuvio instrument, the resolution function $R_{i_M}(y_{i_M}(t))$ strongly depends on the mass of the atomic species [3], which renders fitting of the experimental Compton profiles with combinations of multiple Gaussian profiles for the heavy atomic species unfeasible. So far, only in the case of protons, where the full-width at half maximum (FWHM) of the resolution function accounts for about one-fifth of the FHWM of the typical experimental Compton profile [3], linear combinations of up to three Gaussian components could be successfully fitted to experimental data [12].

Two important experimental factors dictate the choice of instrument geometry in the case of Vesuvio, and both of them are consequences of the kinematic regime in which the neutron Compton scattering takes place. Firstly, the instrument resolution function strongly depends on the kinematics of the scattering process of neutrons of the electron-Volt energy range, and fixing the final energy of scattered neutrons results in a much better instrument resolution volume in the $q - \omega$ space than it would have been in the case of the direct-geometry Vesuvio counterpart. Indeed, direct-geometry neutron instruments, on which attempts have been made to mimic Vesuvio, yielded MANSE spectra with peaks dominated by their respective instrument resolution functions [13, 14]. The second factor acting in favour of the inverted-geometry setup on VESUVIO is the constancy of the neutron detector efficiency in the case when the final neutron energy is fixed.

In the Compton scattering process within the impulse approximation regime, the relationship between the values of the initial ($v_0(t_r)$) and nal ($v_1(t_r)$) velocities of neutrons, measured at the TOF flight, t_r, corresponding to the centre of the recoil peak for a given nucleus of mass M is given by the following formula [3]:

$$\frac{v_1(t_r)}{v_0(t_r)} = \frac{\cos\theta + \sqrt{(M/m)^2 - \sin\theta^2}}{M/m + 1} \qquad (6)$$

Figure 3. TOF spectra, $C(t)$ of LiH and LiD as a function of the scattering angle: LiH, $\theta = 30^o$ (a), LiH, $\theta = 60^o$ (b), LiH, $\theta = 80^o$ (c), LiD, $\theta = 30^o$ (d), LiD, $\theta = 60^o$ (e), and LiD, $\theta = 160^o$ (f). Proton and deuteron recoil peaks are marked in red, and lithium recoil peaks are marked in blue. The respective resolution functions are marked as lighter shades of red and blue, respectively. The total spectra (the sums of the individual recoil peaks) are plotted as thick black lines. See text for details.

If $M = m$, i.e. for scattering from a proton, this equation reduces to $\frac{v_1}{v_0} = \cos(\theta)\big/2$, and $\frac{v_1}{v_0} = 0$ for $\theta = 90^o$. Thus, MANSE measurements for protons are performed only at forward scattering angles, whereas for backscattering, scattering from stationary hydrogen atoms does not occur at all [3]. Moreover, by virtue of the fact that the integral intensity of a peak of a given isotopic species, present in a MANSE spectrum, is proportional to its total bound scattering cross-section, the integral peak intensity of a proton, recorded in forward scattering is typically at least an order of magnitude bigger than its counterparts of other isotopic species. On the whole, the forward-scattering MANSE spectra are dominated by proton peaks, while the heavier isotopic species dominate their backscattering counterparts. In other words, the MANSE technique provides a unique 'kinematic filter' whereby isotopic species heavier than protons can be selectively measured in backscattering.

The dynamic structure factors for solid LiH and LiD are shown in figure 2, and the TOF spectra in figure 3. The recoil peaks of protons, deuterons and lithium nuclei are simulated for the fixed final neutron energy of $E_1 = 4.9$ eV, the initial and final flightpaths of 11 and 0.5 metres, respectively, and the values of scattering angles of 30, 60 and 80 degrees, in the case of the LiH, and 30, 60 and 160 degrees in the case of LiD. Moreover, the effects of the mass and kinematics-dependent resolution functions are incorporated into the simulations. One can see that the values of the energy transfer (measured at the centres of the respective recoil peaks in the dynamic structure factor) vary between 5 and 600 eV for the Compton scattering on protons in LiH, for the scattering angles between 30 and 80 degrees (figure 2, panels a, b, c). In the case of the scattering on heavier masses like deuteron and lithium in LiD, these values are reduced and lie in the range between a fraction of an eV and 40 eV for the scattering angles in the range of 30 to 160 degrees (figure 2, panels d, e, f). In the θ range from 30 to 80 degrees, the magnitudes of the momentum transfer, q, vary from 20 to 500 Å^{-1} and from 20 to 200 Å^{-1}, in the case of the Compton scattering off protons and heavier masses such as Li and deuteron, respectively. Importantly, the 'kinematic filtering' of the MANSE technique is clearly visible in the case of the simulation of the LiH spectra recorded in forward scattering (figure 2, panels a, b, c). The spectra are clearly dominated by the
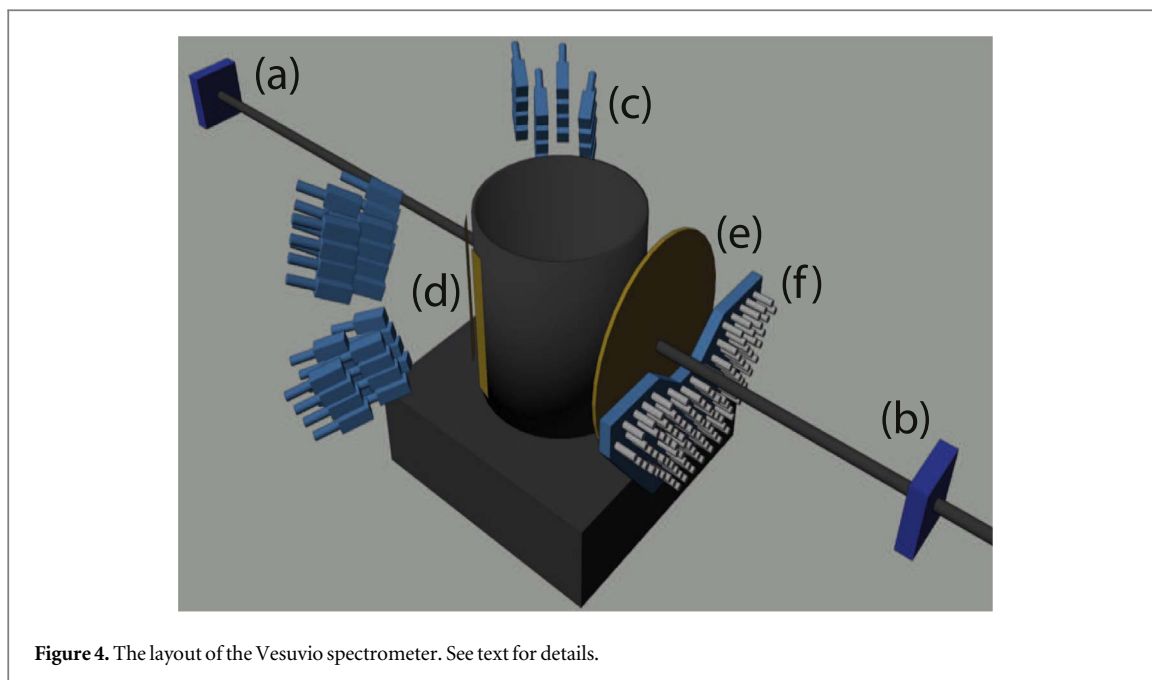
Figure 4. The layout of the Vesuvio spectrometer. See text for details.

contributions from the proton recoil peaks. Moreover, the proton recoil peak intensity clearly decreases with increasing scattering angle, and the peak width increases with the peak becoming increasingly asymmetrically elongated towards the even higher values of the neutron energy transfer. This behaviour is the consequence of the impulse approximation, in which the recoil peak intensity is inversely proportional to the magnitude of the momentum transfer, and the peak width increases linearly with the increasing value of q, keeping the integral intensity of $S(q, \omega)$ of a given nucleus constant, according to the so-called 'sum rule' [1]. At an 80-degree scattering angle, the proton recoil peak is already difficult to observe, as it stretches towards very high ω values, thus requiring a very fine data acquisition resolution at very low TOF values. Closer to the limit 90-degree scattering angle, the proton recoil peak would stretch so far that it would practically vanish into the experimental baseline, rendering its observation practically impossible. The situation is completely different in backscattering. The proton recoil peak is absent, and the shapes of the recoil peaksof lithium can be much better recovered from the spectra as their integral intensities become comparable with the integral intensities of deuterons in LiD. Moreover, as the scattering angle increases towards 160 degrees, the mass resolution improves.

2.2. Vesuvio instrument setup

Having introduced the main concepts and experimental limitations associated with the detection of epithermal neutrons in the Compton scattering process, we are ready to discuss the layout of the Vesuvio spectrometer depicted in figure 4. In doing so, we will consequently adopt an experimentalist's view, referring the readers for detailed descriptions to existing reviews and books [1–6].

One of the distinctive features of the Vesuvio beamline is the concurrency of different types of neutron experiments that can be performed on the same sample without the need for sample material replacement and renewed instrument calibration [1–4]. Thus, Vesuvio simultaneously offers NCS and MANSE, neutron diffraction (ND), neutron resonant capture and transmission analysis (NRCA and NRTA), as well as the incident neutron energy-dependent sample transmission (NT). The last technique is crucial when it comes to the successful planning and data analysis of a MANSE experiment. The role of the NT technique, as employed on Vesuvio, is multifold. It yields transmission curves that can be used in their own right to characterise materials properties [15]. It can be employed for the determination of the shapes of neutron absorption resonances in the NRTA technique. It is also employed to measure the incident neutron spectrum, $I(E_0)$, needed for the MANSE spectra normalisation. Finally, it allows for the measurement of the scattering power of a given sample, which is crucial for the determination of the ratio of the single-to-multiple scattering in the sample, which dictates how much of the multiple neutron scattering correction needs to be taken into account in analysing the MANSE data [16, 17]. Given the multitude of roles that the NT technique plays, it is quite remarkable that, for the successful completion of an NT experiment, essentially only two elements of the beamline hardware are necessary, the incident and transmitted neutron detectors, depicted in figure 4 as blue cuboids labelled, (b) and (a) respectively.

The fact that VESUVIO, in the NCS (or MANSE) mode, works effectively as a 'kinematic filter' dictates how the instrument neutron detection system is set up. In forward scattering, the signals recorded are dominated by the contributions from the neutron Compton scattering off protons. The total bound scattering neutron cross-

section for protons is 82 barns, while for most of the other nuclei, the cross-section values are at least an order of magnitude lower [15]. Thus, forward scattering detectors need to cope with relatively high count rates due to scattering off protons. Additionally, they need to provide excellent resolution, signal-to-background ratio and minimal saturation risk. In order to achieve this demanding specification, Vesuvio employs 64 cerium-doped yttrium aluminium perovskite (YAP) gamma-ray detectors, organised into four detector banks, two right and two left with respect to the incident neutron direction (see figure 4(c)) [1–4]. YAP detectors are designed to function both as neutron and energy selectors. Gold foils, resonantly absorbing scattered neutrons with the final energies, $E_1 = 4.9 \pm 0.15$ eV, are placed on the YAP detector faces. When neutrons, scattered off the sample under investigation into the forward direction, hit the gold foil, gamma-rays are instantaneously produced in a nuclear (n,γ) reaction and subsequently detected using the YAP crystal scintillators. In principle, the forward detection of Compton-scattered neutrons would have stopped at this relatively simple setup stage if it was not for the fact that a gamma background is present inside the Vesuvio blockhouse. Actually, spectra recorded by the YAP detectors in this setup can be directly used in the NRCA technique as implemented on Vesuvio [18]. In this case, gamma rays, produced by resonant neutron absorption followed by gamma-ray emission in the sample material, travel almost instantaneously to the YAP detectors and are recorded as a function of the TOF of the incident neutrons. As the cross-section values for the resonant neutron absorption followed by gamma-ray emission are, in most cases, at least three orders of magnitude larger than the total bound neutron scattering cross-sections, the background signal intensity can be neglected in the NRCA technique. However, the background intensity is comparable to the intensity of the signal due to Compton-scattered neutrons, and background subtraction is necessary in the case of the MANSE technique. To achieve this, gold foils shaped as sections of a cylinder are periodically cycled in and out of the scattered neutron beam by the forward scattering foil changer. At present, on Vesuvio, two periods are used for the forward neutron detection. In these two periods, the motors of the forward scattering foil changer rotate and stop the foils in relative angular positions of -42° and -52° and 45° and 55°, left and right of the incident neutron beam direction, respectively. The duration of the time periods in which the foils remain stationary is determined by the desired signal-to-noise ratio of the recorded spectra and is currently in the region of 5 minutes. At any given moment of time, some YAP detectors are covered by the additional (secondary) gold foils, and the scattered neutrons travel through those foils, hit the primary foils covering the YAP detector faces, and get counted by the data acquisition electronics. At the same time, some other YAP detectors register scattered neutrons that have not traversed the secondary foils. Then, the situation reverses in a subsequent detection period. The final forward scattering TOF spectra are obtained by subtraction of the 'foil-out' and 'foil-in' signals. Two important goals are reached simultaneously in such a 'resonant detection setup'. Firstly, the gamma background signals are subtracted. Secondly, the instrument resolution is greatly improved as the result of the subtraction of two energy resolution functions peaked at the same value of the final neutron energy but having different widths due to different thicknesses of the gold foil covering the YAP detector faces and those that are cycled in and out [1–4].

In order to detect epithermal neutrons backscattered from a sample on Vesuvio, a different neutron detection technique is employed [1–4]. Contrary to the forward scattering, neutrons are detected directly without resorting to gamma-ray detection. Gold foil, strongly and resonantly absorbing neutrons, mounted inside a rotating flat aluminium cylinder (Figure 4(e)), is placed between the sample position and the backscattering detector bank (figure 4(f)). The aluminium cylinder is divided radially into six sections: three with no gold foil, two containing a 0.05 mm thick foil, and one containing a 0.0125 mm thin foil. The cylinder is rotated periodically every 5 minutes (in concert with the periodic motion of the forward neutron analyser foils) in such a way that, for a given period of time, some neutrons scattered off the sample into the backward direction must travel through a thin foil section, other neutrons travel through a thick foil section, and the remainder of neutrons travel through the flat aluminium cylinder section that does not contain the gold foil. Then, for a subsequent period of time, the situation reverses. Currently, the rotating foil changer is programmed to rotate and stop at three different relative angular positions of 232.5°, 292.5°, and 352.5°. The neutron data acquisition is idle at no time, as the final neutron spectra in the TOF domain are defined as differences between the signals recorded in periods when the gold foil is placed between the sample and detector position and background signals being recorded in periods when no gold foil is placed between the sample and a given section of detectors. Such a setup guarantees a correct background subtraction even if the incident neutron beam intensity varies in time. It also enables different combinations of signals and background signals to be subtracted: (i) 'thick foil signals' minus 'background', (ii) 'thin foil signals' minus 'background', and (iii) 'thick foil signals' minus 'thin foil signals'. As we mentioned in section 2.1, any given scattering intensity recorded by an instrument is inextricably intertwined with a finite amount of the instrument resolution. This is especially visible in the case of the detection of backscattered neutrons on Vesuvio, as the Vesuvio resolution function in backscattering is dominated by the contribution from the gold foil final neutron energy analyser [1–4]. The three different signal differencing schemes will lead to three different signal intensities obtained at the expense of three different amounts of the instrument resolution. In the first scheme (referred to as the 'thick difference'), the intensity of

the signal will be the highest with the poorest instrument resolution. In the second scheme, the signal intensity will decrease relatively to the first scheme, while the resolution will improve. In the third detection scheme, the signal intensity will be the lowest, but the resolution will be the best of the three schemes, as the long tails of the energy resolution function due to the resonant neutron absorption will reduce resulting in a much narrower energy resolution function peak shape [1–4]. This last detection scheme, nicknamed 'double differencing', is the preferred mode of Vesuvio MANSE operation at backscattering. Similarly to the situation in forward scattering, in backscattering on Vesuvio, more than one neutron technique can be employed. The elastically scattered neutrons diffracted from the sample under investigation can be directly detected during the 'foil-out' detection periods and produce high-resolution diffraction patterns in the time-of-flight [19, 20].

2.3. MANSE data analysis

In the spirit of this review, here we will only describe the main ideas behind the major building blocks of the MANSE data analysis from a practical viewpoint. In doing so, we will focus on the analysis of data obtained for composite systems with average recoil peak shapes that are very well approximated by Gaussian NMDs with underlying harmonic interatomic potentials. Thus, we will bid farewell to the entire branch of data analysis devoted to detailed peak shape analysis beyond a simple Gaussian and numerical reconstruction of the associated shape of the potential of the mean force experienced by a given nuclear species described in detail in specialised review articles and book chapters [1–4].

The basic data analysis philosophy reflects the instrument setup described in the previous section. It provides two different modes of analysis, one for data recorded in backscattering and one for forward scattering data. There is, however, a common goal of both modes of data analysis: to obtain the average values of standard deviations of NMDs (hereinafter referred to as 'peak widths') and relative peak intensities (or, for short, 'peak intensities'). This task is achieved by fitting the equation (5) for the count rate in the TOF domain. In doing so, the relative peak intensities can be tied together according to the sample stoichiometry (a technique referred to as 'stoichiometric fixing') in order to increase the precision of the fitting of the peak widths. Alternatively, the peak intensities can be set free in fitting to obtain the sample composition. As we shall see in a more detailed description provided in sections 3 and 3.5, peak widths are related to a plethora of physical and chemical phenomena and linked to a number of important observables.

Besides sharing the same observables, forward and backward MANSE data analysis also share a number of basic data treatment steps. Raw data recorded in both forward and backscattering usually consists of a series of overlapping recoil peaks in the TOF domain. Even for samples consisting of atomic species with nuclei with largely different masses (like deuterons and lithium in figure 3), a complete peak separation will be only achieved for relatively small numbers of detectors, and analysing isolated recoil peaks of individual masses will not be warranted due to poor signal-to-noise ratio, even if the signals of different detectors are grouped. Two other optimal strategies are employed in practice. The first relies on fitting TOF spectra detector-by-detector (i.e., sequentially), obtaining the values of peak widths and intensities for the individual detectors, and averaging the fitted values of peak widths and intensities over all detector sets. The second strategy relies on grouping unit-area-normalised signals recorded by different detectors and fitting them with a synthetic curve obtained by mimicking the procedure the data is subject to. This second method is nicknamed 'Cumulative Angle-Averaged Data' (or CAAD) analysis [21].

Both data analysis strategies can be straightforwardly applied to raw data recorded in backscattering in the case of a small (of the order of a few per cent) value of the scattering power. In such a case, the contribution from multiple scattering (MS) to the signals recorded by individual detectors is negligible [16, 17]. As we have seen from our description of the Vesuvio instrument setup in the previous subsection, the estimation of the scattering power is a relatively trivial task owing to the ability of Vesuvio to perform NT and MANSE measurements concurrently. Thus, the value of the scattering power of the sample can be assessed before the actual MANSE data analysis starts. In the case when the scattering power of the sample is of the order of ten per cent or higher, the MS correction needs to be applied in the following procedure [5].

- During the initial fitting procedure, the expression 5 for the count rate in the TOF domain is fitted to raw, uncorrected data sequentially (detector-by-detector) taking into account the kinematics of the neutron Compton scattering process and sets of parameters, $(L_0, L_1, \theta, t_0)_n$, obtained in the instrument calibration procedure individually for each detector number, n. As a result of this step, the values of peak widths and intensities for the individual detectors are obtained.

- The fitted values of peak widths and intensities, obtained for individual detectors in the previous step, are averaged over all detector sets, and the averaged values for input to the MS correction procedure. The MS correction is calculated for individual detectors based on the average peak width and peak intensity values, the kinematics of the neutron Compton scattering process and sets of parameters, $(L_0, L_1, \theta, t_0)_n$, obtained in the

instrument calibration procedure individually for each detector number, n. The validity of this step relies on the feature of the MS correction for the neutron Compton scattering, whereby the shapes of the MS corrections, calculated for individual detectors, are much less sensitive to small deviations in the values of peak widths and intensities but more sensitive to the kinematics and instrument calibration [16].

- The MS corrections, calculated individually for each detector, are subtracted sequentially from the raw data, and the corrected data are fitted again to obtain the second approximation for the average values of peak widths and intensities;

- The average values of peak widths and intensities obtained in the second approximation are input to the procedure calculating the MS correction, and the procedure repeats until a desired degree of self-consistency and numerical parameter convergence is attained.

In the case of the data recorded in forward scattering, however, even in the presence of a negligible amount of multiple scattering, one more important raw data correction needs to be applied: the correction to account for the sample composition-dependent gamma background [5, 22]. This correction is a direct consequence of the current Vesuvio instrument setup. Forward scattering detectors, as described in the previous section, detect gamma rays instead of neutrons. With two sets of gold foils covering these detectors, a situation may occasionally arise whereby gamma rays originating from the moving foils, positioned some distance in front of a given YAP detector, reach the detector practically instantaneously, wrongly signalling the arrival of a neutron at the position of the detector [22]. This artefact of the YAP detection introduces artificial recoil peaks into the TOF spectra centred at TOF values shorter than those expected from the 'normal' process whereby a neutron scattered off a sample produces gamma rays in the gold foil placed on the YAP detector face [22]. However, knowing the sample composition, the values of $(L_0, \ L_1, \ \theta, \ t_0)_n$, obtained in the instrument calibration procedure individually for each detector number, n, and having some idea about the correct values of the peak widths and intensities from an initial pass of fitting the expression 5 for the count rate in the TOF domain to raw, uncorrected data sequentially (detector-by-detector), allows for analytical correction of the sample-dependent gamma background [5, 22]. On the whole, the following procedure of forward scattering data treatment can be envisaged [5]:

- During the initial fitting procedure, the expression 5 for the count rate in the TOF domain is fitted to raw, uncorrected data sequentially (detector-by-detector) taking into account the kinematics of the neutron Compton scattering process and sets of parameters, $(L_0, \ L_1, \ \theta, \ t_0)_n$, obtained in the instrument calibration procedure individually for each detector number, n. As a result of this step, the values of peak widths and intensities for the individual detectors are obtained.

- The fitted values of peak widths and intensities, obtained for individual detectors in the previous step, are averaged over all detector sets, and the averaged values for input to the sample-dependent gamma background (GB) correction procedure and the MS correction procedure. Both GB and MS corrections are calculated for individual detectors based on the average peak width and peak intensity values, the kinematics of the neutron Compton scattering process and sets of parameters, $(L_0, \ L_1, \ \theta, \ t_0)_n$, obtained in the instrument calibration procedure individually for each detector number, n.

- The GB and MS corrections, calculated individually for each detector, are subtracted sequentially from the raw data recorded by each detector, and the corrected data are fitted again to obtain the second approximation for the average values of peak widths and intensities;

- The average values of peak widths and intensities obtained in the second approximation are input to the procedures calculating the GB and MS corrections, and the procedure repeats until a desired degree of self-consistency and numerical parameter convergence is attained.

Following the procedure itemised above, two choices are possible for further treatment of the corrected forward scattering data. Both of them are motivated by the need to obtain data with a much-improved signal-to-noise ratio compared to their counterparts recorded by individual detectors. In the first case, the data are subject to the CAAD procedure [21]. In the second case, recoil peaks of a chosen nuclear species can be isolated in the TOF domain by subtracting from each spectrum recorded by an individual detector the synthetic signals representing the fitted recoil peaks other than those of the isolated nuclear species [5]. The isolated recoil peaks are subsequently transformed (detector-by-detector) from the TOF to the y-space domain of the chosen nuclear species and then focused in this space in order to obtain a nuclear momentum distribution, which can be then fitted much more accurately in the y-space domain in order to obtain a more precise value of the momentum distribution width, σ [5].

At present, the combined signal-to-noise ratio and the nuclear mass-separation achievable on the VESUVIO spectrometer allow obtaining the values of NMD widths with a precision as high as 1% for hydrogen and 10% for heavier nuclei [1–4, 23, 24].

3. Nuclear quantum effects

3.1. Preliminary remarks

The term 'Nuclear Quantum Effects' (NQEs) encompasses a wide range of different physical and chemical phenomena [1–4, 23–26]. However, one can argue that, to a material scientist, this term would be linked to the quantum description of the motion of atoms in condensed matter systems and molecules and the ramifications that this description has for physical and chemical properties of materials. These local equilibrium positions of atoms may be fixed in space, at least when viewed in the time window of an experimental technique employed to look at them, a situation that can be referred to as 'an operational definition of a solid' [23]. In other cases, the equilibrium positions may change during the observation time of a given experimental technique, as atoms perform motions that are superpositions of translations, rotations, and vibrations, a situation encountered in liquid or gaseous systems. This operational division between the solid and non-solid environment may seem to create a conceptual difficulty. However, one can always decompose the motion of an object (a molecule, for that matter) into its centre-of-mass translation, rotation, and vibration of its constituent atoms, with its kinetic energy factored as a sum of the kinetic energies of the three respective types of motion. Moreover, in most cases, the atomic kinetic energy of the translation and rotation is almost two orders of magnitude smaller than the kinetic energy associated with atomic vibration. This very important approximation has two far-reaching consequences. Firstly, it relates the bulk of atomic motion to a periodic, oscillatory phenomenon whereby atoms perform small-amplitude vibrations around their local equilibrium positions, which can be physically described using the theory of the harmonic oscillator (HO). Secondly and most importantly, this approximation creates an easy conceptual link between atomic motion and the chemical environment. In what follows, we will explore this link using the fact that atoms are quantum objects. To this end, before delving into the quantum harmonic oscillator (QHO), we will briefly introduce some basic, however important for a chemist, facts and properties known from the classical HO mechanics.

3.2. Classical harmonic oscillator

There are many different pictorial representations of a classical HO: a ball rolling without friction in a curved dish or a pendulum swinging frictionlessly back and forth. However, the most iconic picture is that of a single mass connected to a spring performing a motion on a single-dimensional axis. In such a 'mass-and-spring' system, the mass, m, when displaced from its equilibrium position, x_0, experiences a restoring force, F. According to Hooke's law, the restoring force has a magnitude proportional to the displacement, x, from the equilibrium length x_0, and acts in the opposite direction to the displacement vector, $F = -kx$, where $k = m\omega^2$ is the force constant, which reflects the stiffness of the spring, and ω is the frequency of vibration. The potential energy for such a system, V increases quadratically with the displacement, $V = \frac{1}{2}kx^2$. The momentum associated with the classical HO, p is just the product of the mass of the vibrating particle m and its velocity $\frac{dx}{dt}$, $p = m\frac{dx}{dt}$. During the harmonic motion, the total energy, E, is being shifted continuously between potential energy, V, stored in the spring and kinetic energy, $T = \frac{p^2}{2m}$. The total HO energy is equal to the maximum potential energy at the so-called classical turning points when $x = a$, and thus $V = \frac{1}{2}ka^2$ (figure 5).

Importantly, a classical particle in a 'mass-and-spring' can never be found beyond its turning points, a, and its energy depends only on how far the turning points are from its equilibrium position. Secondly, the lowest energy that a particle in such a system may have is zero, being at rest at its equilibrium position at the bottom of the potential well. Thirdly, no matter how big the energy of a particle is in a classical HO, the probability of finding it is highest near the turning points and lowest at the equilibrium position. As we will see from the comparison between the classical and quantum HO, none of these characteristic features describe the harmonic motion of a quantum particle at all. In fact, they are completely turned upside down in the quantum world. There are, however, some other properties of a classical HO that survive this comparison. The first of them is the fact that one basic theorem of classical mechanics applies both to the classical and quantum HO, the virial theorem. The virial theorem states that the (time-averaged) kinetic and potential energies of a HO are qual, $\langle T \rangle = \langle V \rangle$, and in consequence $\langle T \rangle = \frac{1}{2}E$. The second important feature is that, both in the classical and quantum description, one can relate the force constant k and the frequency of the vibration, ω, via the concept of a reduced mass of a vibrating object, m, and write $\omega = \sqrt{\frac{k}{m}}$. The reduced mass, m, is a very useful concept that allows us to view a multi-body system as a single particle and, consequently, to separate the vibration and rotation of the
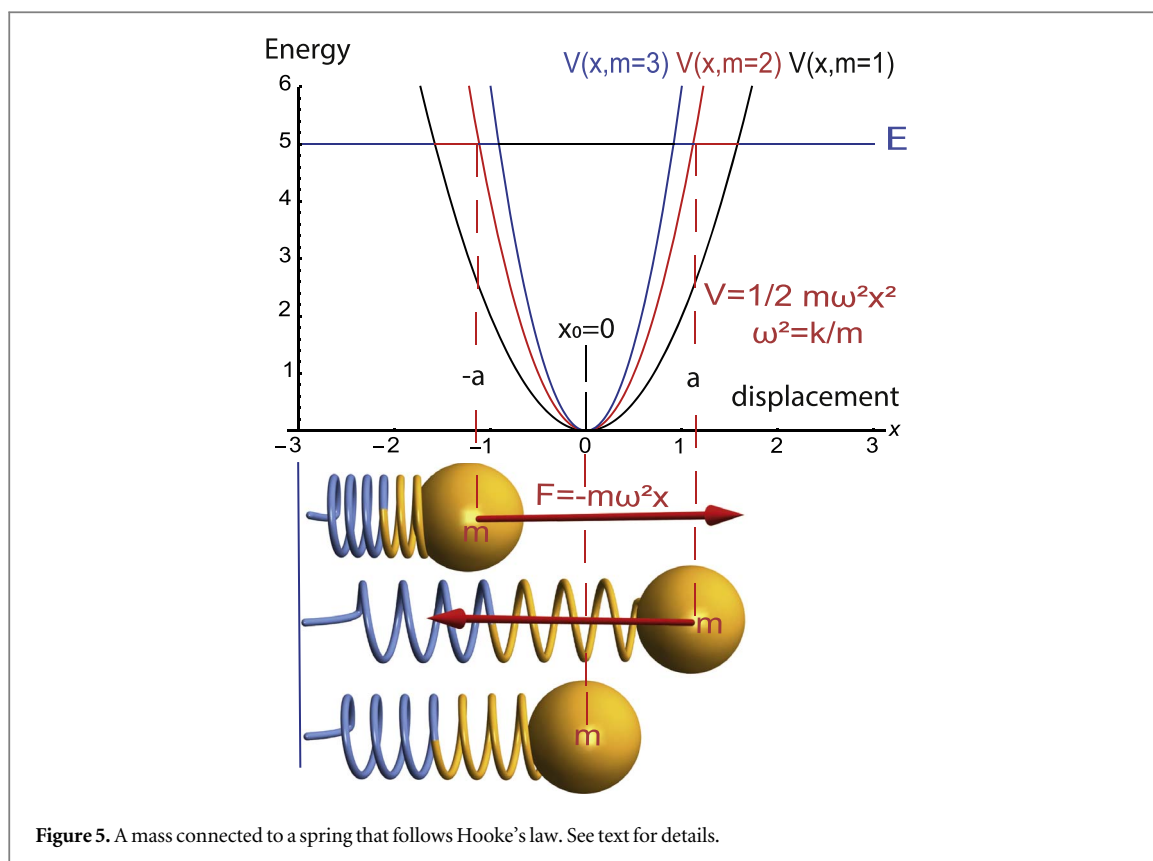
Figure 5. A mass connected to a spring that follows Hooke's law. See text for details.

particle from the displacement of the centre of mass. This approach greatly simplifies many calculations and problems. In its most pictorial representation, for studying molecular vibration of diatomic molecules, the reduced mass m is defined as $m = \dfrac{m_1\,m_2}{m_1 + m_2}$, where the respective masses of atoms A and B are m_1 and m_2. In its extreme case, for $m_1 \gg m_2$, $m = m_1$, we retrieve the picture of a single particle of mass m_1 vibrating on a spring, as depicted in figure 5, and an extreme, yet very useful, representation of a two-body system as a single-body one.

The model of a classical particle in a 'mass-and-spring' system, governed by Hooke's Law, is an excellent approximation for the vibrational oscillations of molecules. Strikingly, one does not need to know the origin of the magnitude of the force constant, k, to be able to calculate thy atomic vibrational dynamics. The magnitude of k can be simply yielded by an experiment or taken from tabulated values in books without resorting to quantum mechanical calculations. It has been tantamount to the success of long-celebrated models, such as the one by Born and Karman, to state that one can obtain vibration frequencies by solving algebraic equations for systems of classical objects represented by a set of 'balls and springs', effectively saying farewell to quantum mechanics and stating that the force constants are just external model parameters that depend upon the nature of chemical bonds. Furthermore, we can build up our intuition about atomic dynamics just by resorting to the observation that it is the electron distribution between the two positively charged nuclei that holds them together. Consequently, a double bond with more electrons has a larger force constant (and hence the vibration frequency) than a single bond, and the nuclei are held together more tightly. Moreover, for the same electronic density between the nuclei in a bond, the greater the mass of a nucleus in a bond, the lower the bond vibration frequency, an effect which is tantamount to a whole collection of phenomena referred to as 'isotope effects' in chemistry. Closing our discussion, one has to emphasise that a stiff bond with a large force constant is not necessarily a strong bond with a large dissociation energy. In other words, a harmonic bond can never be broken, as the HO model has no concept of the bond dissociation energy built in. This fundamental flaw is shared by both classical and quantum HO models, as both of them predict a restoring force always to keep a bond together.

3.3. Quantum harmonic oscillator

Quantum mechanics (QM) enters the scene if one wants to account for the magnitude of interatomic force constants, as opposed to just 'plugging' them into models taken from classical mechanics. A detailed description of the 'ab initio' methodology of the electronic structure calculation is beyond the scope of this review. Here, we remark only that, in essence, the solution to the problem of solving the electronic structure in condensed matter systems and molecules relies on a series of approximations applied to the most basic QM-object, the wave function, representing a mathematical description of the quantum state of an isolated quantum system. The

main one, referred to as the Born-Oppenheimer (BO) approximation, is the assumption that the motion of atomic nuclei and electrons in a molecule can be separated. Operationally, BO stands for a two-step equation-solving procedure. In the first step, the electronic Schrödinger equation is solved, yielding the wave function depending on electrons only. During this solution, the nuclei are fixed in a certain configuration. In the second step of the BO approximation, this function serves as a potential in a Schrödinger equation containing only the nuclei. To this end, it would be perhaps intuitive to describe the nuclei using wave functions and the Schrödinger equation. Thus, it may come as a surprise that both in the classical (CMD) and Born–Oppenheimer Molecular Dynamics methods (BOMD), the trajectories of atoms are determined by numerically solving Newton's equations of motion for a system of classical interacting particles. Moreover, perhaps the most popular method to account for the NQEs, harmonic lattice dynamics (HLD), does not compute the trajectories of atoms at all and accounts for their kinetic energy of motion solely by solving the eigenproblem of the dynamical matrix.

As already mentioned above, the same expression effectively controls the relation between the mass, the force constant and the oscillation frequency of a given normal mode, both in the case of the classical and the quantum HO. However, the energy of the QHO is limited to certain values. The allowed quantised energy levels are equally spaced and are related to the oscillator frequencies ω by $E_n = \left(n + \frac{1}{2}\right)\hbar\omega$ with $n = 0, 1, 2, 3,$ $\cdots \infty$ and $\hbar$ being the Planck's constant (figure 6).

Unlike in the case of the classical HO, if atoms in bonds are described by the QHO model, we cannot specify the exact position and momentum of the atoms as a function of time. Instead, for any given quantum state of the QHO numbered n, we can only calculate the average displacement (momentum) and the mean square displacement (momentum) of the atoms in bonds relative to their equilibrium positions. For any value of n, the average displacement, $\langle x \rangle_n$, and average momentum, $\langle p \rangle_n$, yield zero values, whereby the mean square displacement $\langle x^2 \rangle_n$, and the mean square momentum, $\langle p^2 \rangle_n$ are finite, positive numbers, reading $\langle x^2 \rangle_n = \left(n + \frac{1}{2}\right)\frac{\hbar}{\mu\omega}$, and $\langle p^2 \rangle_n = \left(n + \frac{1}{2}\right)\hbar\mu\omega$, respectively (with μ being the reduced mass). This mathematical result is the consequence of the fact that a QHO, in stark contrast to the classical HO, in its lowest-energy state (with $n = 0$), has a non-zero value of the total energy, $E_0 = \frac{1}{2}\hbar\omega$. This phenomenon is referred to as zero-point energy (ZPE) and is the most iconic manifestation of the NQEs. Moreover, owing to the virial theorem, the average values of potential and kinetic energy for the QHO state with $n = 0$ are equal, with $\langle T \rangle = \langle V \rangle = \frac{1}{2}E_0 = \frac{1}{4}\hbar\omega$.

3.4. Turning points and tunnelling

The maximum extension of a classical HO can be calculated using the concept of the classical turning points because, at the maximum extension, all the QHE energy is in the form of potential energy. For a QHO, however, at the classical turning point positions, the oscillator still has kinetic energy and momentum to continue to extend beyond these points. Mathematically, the wave functions and the squares of the magnitudes of the wave functions of the QHO extend beyond the classical turning point positions, i.e. beyond where the particle can be according to classical mechanics (figure 6) [27]. Thus, for any eigenstate, the QHO has a finite probability of having a displacement (amplitude of vibration) that is larger than what is classically possible. This is tantamount to yet another iconic NQE effect, the nuclear quantum tunnelling (NQT).

Let us calculate the probabilities of finding particles between the classical turning points, $-a, a$, for different QHO states and normalise them by their counterparts calculated over the entire displacement domain, x:
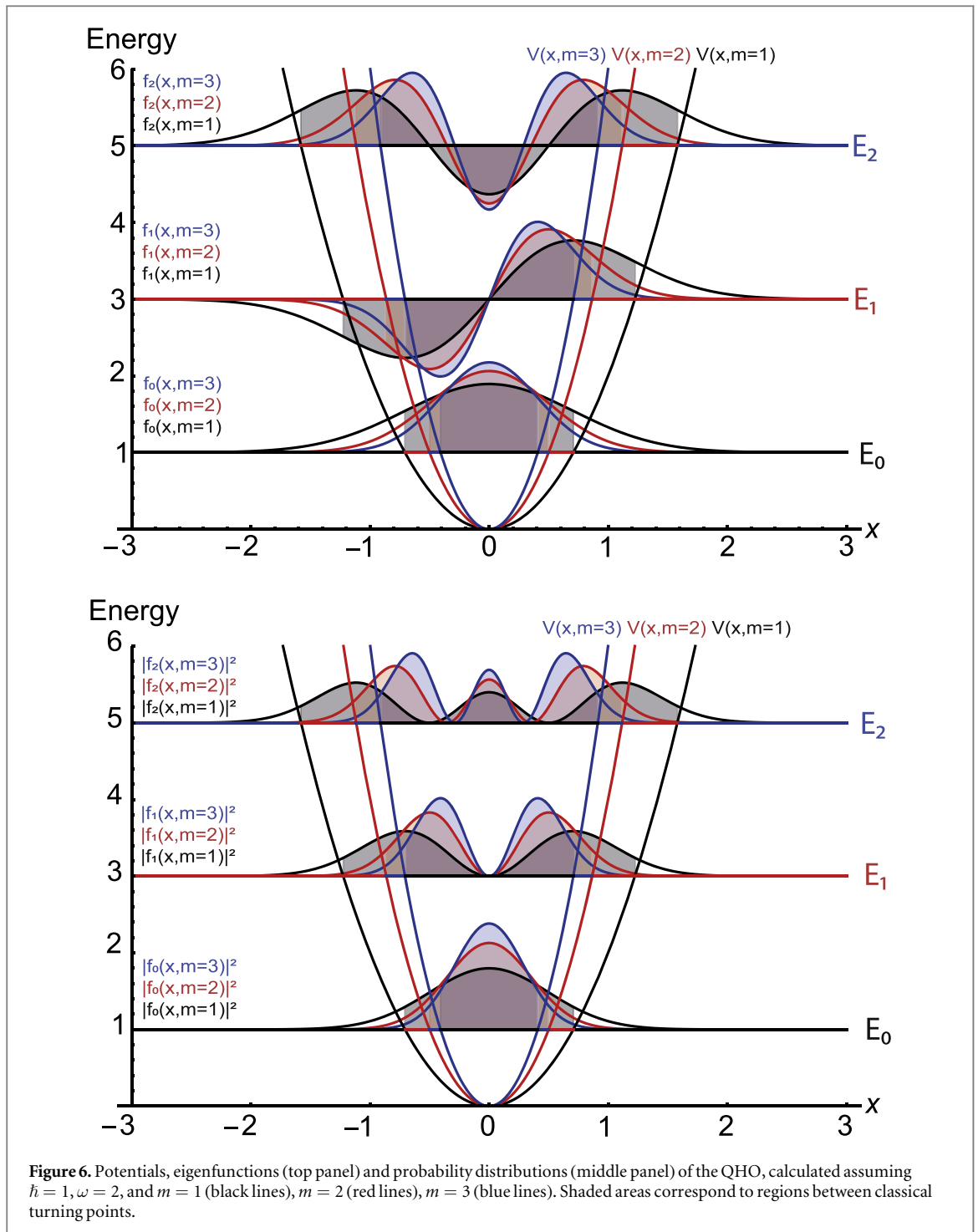
$$p_{cl}(a) = \frac{\int_{-a}^{a} |\psi_n(x, m, \omega)|^2 dx}{\int_{-\infty}^{\infty} |\psi_n(x, m, \omega)|^2 dx} \tag{7}$$

where $\psi_n(x, m, \omega)$ is a QHO eigenfunction corresponding to a QHO state n, m is the particle mass, and ω is the frequency of vibration.

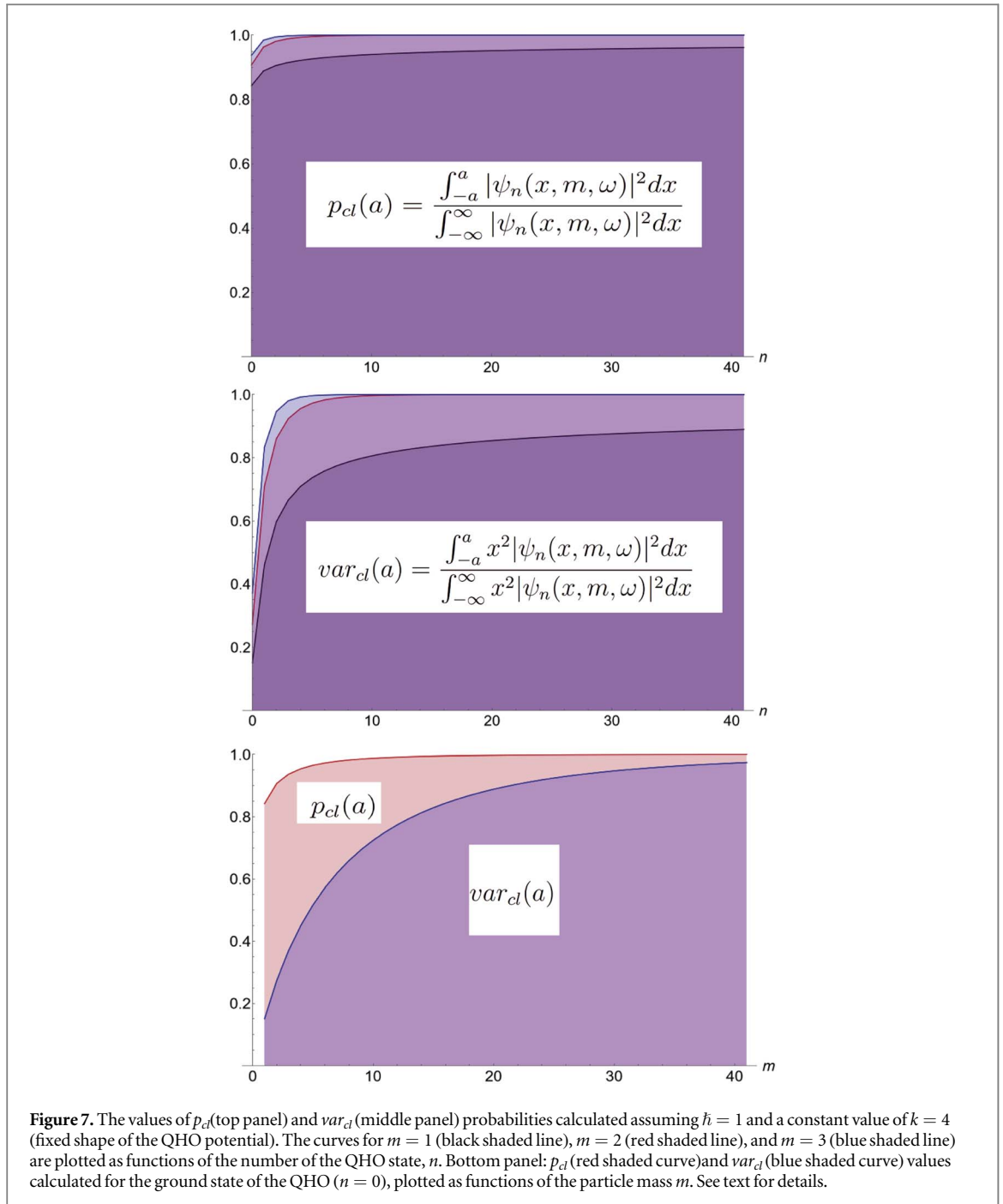Similarly, we can define the variances of the position distributions:

$$var_{cl}(a) = \frac{\int_{-a}^{a} x^2 |\psi_n(x, m, \omega)|^2 dx}{\int_{-\infty}^{\infty} x^2 |\psi_n(x, m, \omega)|^2 dx} \tag{8}$$

The classical turning points can be calculated by two different computational routes. In the first route, one fixes the values of m and ω and solves the equation $\frac{1}{2}m\omega^2 a^2 = \left(n + \frac{1}{2}\right)\hbar\omega$ for a given value of n. This produces a series of potential curves with associated wave functions. As the values of m and ω increase, both the turning points and the regions of the wave functions with non-zero intensities move closer to the equilibrium positions (see figure 6). The net result is that the values of both p_{cl} and var_{cl} are rendered independent of the values of m and

Figure 6. Potentials, eigenfunctions (top panel) and probability distributions (middle panel) of the QHO, calculated assuming $\hbar = 1$, $\omega = 2$, and $m = 1$ (black lines), $m = 2$ (red lines), $m = 3$ (blue lines). Shaded areas correspond to regions between classical turning points.

ω and only dependent on the value of n. This computational route is thus a nice illustration of the correspondence principle, whereby as n grows, one retrieves classical values of probabilities and p_{cl} and var_{cl} tend to unity (see the top and middle panel plots in figure 7).

In the second computational route, one fixes the magnitude of the force constant, $k = m\omega^2$, so that the turning points are calculated for a fixed potential shape and the values of m and ω change concurrently so as to satisfy $k = m\omega^2 = const$. This is a natural illustration of the isotope effects in chemistry, whereby the change of the isotopic species does not affect the value of k (which is solely governed by the electronic density around the nuclear species), but it changes the value of m and thus the value of ω. The trends reproduced by this computational route are shown in the top and middle panels in figure 7, for p_{cl} and var_{cl}, respectively, for three different values of mass, $m = 1$, $m = 2$, and $m = 3$, and in the bottom panel of figure 7, for a wider range of mass values. One can see quite clearly that, as the particle mass increases, the classical value of p_{cl} and var_{cl} are attained much more quickly as a function of n. On the whole, these trends reproduce yet another way of obtaining the

Figure 7. The values of p_{cl}(top panel) and var_{cl} (middle panel) probabilities calculated assuming $\hbar = 1$ and a constant value of $k = 4$ (fixed shape of the QHO potential). The curves for $m = 1$ (black shaded line), $m = 2$ (red shaded line), and $m = 3$ (blue shaded line) are plotted as functions of the number of the QHO state, n. Bottom panel: p_{cl} (red shaded curve)and var_{cl} (blue shaded curve) values calculated for the ground state of the QHO ($n = 0$), plotted as functions of the particle mass m. See text for details.

quantum-to-classical transition, whereby the higher the particle mass, the closer it is to the classical limit for a given value of n.

    Whereas the degree of 'quantumness' of a given QHO state can be readily quantified in the position representation, this task is much less obvious in the momentum representation. One of the main reasons for this difficulty is that, in the momentum representation, a Fourier transformed potential, $V(p)$ is convoluted with the wave function $\psi(p)$ as the Schrödinger equation becomes an integral equation [28]. Thus, the task of finding the counterparts of the classical turning points for the QHO in the momentum representation and computing the values of the probability of finding a quantum particle in the classically forbidden region is much more complicated. However, due to the symmetry of the Hamiltonian of the QHO with respect to the Fourier transformation, the QHO eigenfunctions in the momentum representation have the same functional form (and thus the same symmetry) as their counterparts in the position representation. In particular, the solutions of the Schrödinger equation for the QHO in momentum representation are obtained from those in position representation by replacement $x \rightarrow p$ and $m \rightarrow \frac{1}{m\omega^2}$. Thus, instead of delving into the complicated and rather counter-intuitive mathematics of the Schrödinger equation in momentum representation, one can use the symmetry of the QHO representation in quantum mechanics together with the Heisenberg uncertainty

principle to build some intuition about the properties of QHO momentum distributions. For a given state of the QHO, $\langle x^2 \rangle_n \langle p^2 \rangle_n = \left(n + \frac{1}{2} \right)^2 \hbar^2$, and the variances of the position and momentum distributions are inversely proportional. Thus, the overall trend, as far as the momentum representation is concerned, will be that for states with a higher degree of 'quantumness', the value of the variance of the momentum distribution will be larger than a classical prediction. Thus, a quantum delocalisation in position representation will lead to concomitant localisation in position representation.

The results shown in figure 7 are important in the context of the temperature dependence. As the temperature increases, the population of QHO eigenstates with $n > 0$ is governed by the ratio of the energy of the vibration $\hbar\omega$ and the thermal energy k_{BT} (where k_B is the Boltzmann constant) in the Boltzmann energy level population factor. Importantly, the typical energy of vibration of hydrogen in chemical bonds is much higher than k_{BT} for T up to room temperature, and thus, nearly 100% of the total energy of hydrogen vibration is concentrated in the ground QHO states. For heavier atomic species and at higher temperatures, their quantum states will be represented by density matrices that will always have contributions from the ground and excited-state wave functions. However, in light of the results shown in figure 7, nearly all of these states will have a non-negligible quantum character. Thus, methods that rely on the classical picture of nuclei and compute the values of forces acting on nuclei by solving the electronic structure problem using the Schrödinger equation (such as HLD and BOMD) will tend to underestimate the root-mean-square displacements, and concomitantly, overestimate the root-mean-square nuclear momenta. This has important ramifications for the theoretical modelling of chemical properties of materials, as in some situations, a larger amplitude vibration can enhance the chemical reactivity [27]. Moreover, this result shows how important for the appropriate modelling of chemical properties of materials are methods based on quantum treatment of both electronic and nuclear degrees of freedom, such as path-integral molecular dynamics (PIMD), a method capable of accounting for nuclear quantum delocalisation (NQD), coherence (NQC) and tunnelling (NQT) [24, 26].

3.5. Nuclear quantum effects as observed by MANSE

In the case of a nucleus of mass M in equilibrium with the environment at temperature T whose dynamics can be described by the isotropic quantum harmonic oscillator theory, the recoil peak has a Gaussian shape with the value of the standard deviation σ_m given by [1, 3]:

$$\sigma_m^2 = \frac{m}{\hbar^2} \int_0^\infty G_m(\omega) \frac{\hbar\omega}{2} \coth\left(\frac{\hbar\omega}{2k_B T} \right) d\omega. \tag{9}$$

where $G_M(\omega)$ is a partial (atom-projected) vibrational density of states (pVDoS), $\coth\left(\frac{\hbar\omega}{2k_B T} \right)$ is the Boltzmann factor, which represents the temperature-dependent population of vibrational levels of the quantum harmonic oscillator, and k_B is the Boltzmann constant. Equation (9), written in a zero-temperature limit, reads $\sigma_M^2(T=0) = \frac{\hbar M}{2} \int_0^\infty \omega G_M(\omega) d\omega$, and serves as a very useful tool for the understanding of the link between the pVDoS, the average NMD width, and the ZPE-dominated NQEs. Namely, assuming that the pVDoS of a given nucleus is normalised to unity, $\sigma_M^2(T=0)$ can be interpreted as the first moment of the atom-projected VDoS, or in other words, the centre-of-gravity (weighted-mean) frequency of the pVDoS distribution.

Recalling that $\omega = \sqrt{\frac{k}{M}}$, one can relate σ_M^2 to the force-constant of a 'nano-spring' representing the binding force of the confining potential of the recoiling nucleus of mass M. It is important to note that the concept of the NMD width allows us here to effectively replace the whole set of QHOs constituting a pVDoS for a given atomic species of mass M with a single QHO having an effective frequency ω_M that is centred at the centre-of-gravity of Boltzmann population-weighted pVDoS. In this mean-field picture, the value of the average force constant, k, can be obtained from the value of an NMD width by employing the theory of the mean force function (MF) [29]. In the case of an isotropic harmonic potential, the MF is linear with atomic displacement, with force constant magnitude k for a nucleus of mass M at temperature T given by [29]:

$$k = k_B T \sigma_M^2 - \frac{M k_B^2 T^2}{\hbar^2}. \tag{10}$$

Equations (9) and (10) can be used to compare experimental values with their counterparts obtained from *ab initio* predictions. The values of NMD widths obtained from harmonic lattice dynamics or molecular dynamics simulations will generally differ from their experimental counterparts due to the different amount of local binding (or confinement) of a given atomic species predicted by theory. In the extreme case of no binding (and no confinement), one can obtain the theoretical limit for an NMD width of a given nucleus of mass m without resorting to quantum mechanics and using the classical limit of a Maxwell-Boltzmann (MB) distribution at temperature T for a three-dimensional system obeying the equipartition theorem, $3k_B T/2 = 3\hbar^2 \sigma_{cl}^2 / 2M$ [3]:
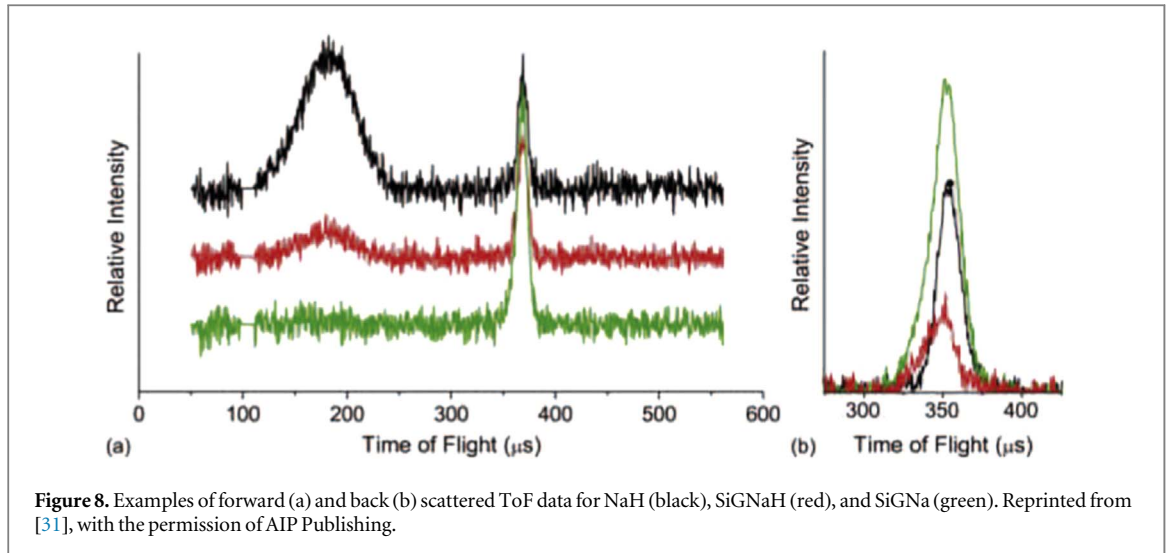
Figure 8. Examples of forward (a) and back (b) scattered ToF data for NaH (black), SiGNaH (red), and SiGNa (green). Reprinted from [31], with the permission of AIP Publishing.

$$\sigma_{cl} = \frac{\sqrt{Mk_B T}}{\hbar}. \tag{11}$$

The value of the σ_{cl} provides a *lower* bound to any possible value of σ_M. As chemical binding and physical confinement lead to an increase in the values of the kinetic energy (and NMD width) of a given atomic species, one can define the measure of the confinement-induced increase in the value of nuclear kinetic energy using the variable of *Quantum-energy Excess* (QE) [30]:

$$QE = \frac{\sigma_M^2}{\sigma_{cl}^2} = \frac{\hbar^2}{Mk_B T}\sigma_M^2 \tag{12}$$

Importantly, as the classical limit is approached by increasing the temperature, both the experimental value σ_M and the classical equivalent σ_{cl} adopt the same linear temperature dependence (QE = 1). Thus, the effect of the local binding environment and concomitant confinement of a nucleus can be translated into the language of thermodynamics, introducing 'the effective nuclear quantum temperature', T_{eff}, that can be defined as $T_{eff} = \frac{\sigma_M^2 \hbar^2}{Mk_B T}$. As shown by the recent MANSE study on the caesium hydrogen sulfide, CsHSO$_4$, the QE as the measure of NQEs can bring surprises. Intuitively, one would assume that the heaviest nuclear species, caesium, will remain 'classical' at all temperatures and the lightest ones, hydrogen, will exhibit NQEs even above ambient conditions. However, at a temperature as low as 10K, the QE of the sulphur is higher than the QE of the oxygen if one takes into account the effects of binding and confinement. This result shows us how the tetrahedral binding environment around sulfur atoms increases the NQEs relative to the peripheral location of oxygen atoms within a given SO$_4$ unit [30].

4. Case studies in nanocomposites

4.1. From bulk material to encapsulated nanoparticles in amorphous silica gel

We open our discussion with the MANSE study of elemental sodium and sodium hydride nanoparticles in an amorphous silica-gel matrix (SiGNaH) [31]. SiGNa consists of particulate, amorphous Na metal dispersed in the nanoscale pores of the silica gel framework. Exposure to hydrogen gas in order to prepare SiGNaH does not damage the silica framework. Instead, isolated particles of crystalline NaH on the order of 20–50 nm are formed [32].

Figure 8 shows examples of TOF MANSE data collected in forward (a) and (b) backscattering geometry on the VESUVIO spectrometer for NaH, SiGNaH, and SiGNa. In forward scattering, one can clearly distinguish two regions in the TOF spectra: (i) an intense and broad peak, stretching from ca. 100 to ca. 300 microseconds of the TOF, due to scattering off protons (clearly absent in the case of the SiGNa sample), and (ii) a narrow peak representing the sum of MANSE response functions from heavier nuclei, Na and Si, as well as the response function of the aluminium sample container. In backscattering, the hydrogen peak is missing due to kinematic constraints imposed on the billiard-ball type of neutron Compton scattering. (No single-scattering occurs of neutrons off protons due to the nearly equal mass of both of the species).

Clearly, the proton peak can be easily isolated (by simply cropping the MANSE spectra in most cases) for further treatment in order to extract the nuclear quantum observables. The results of this procedure are shown
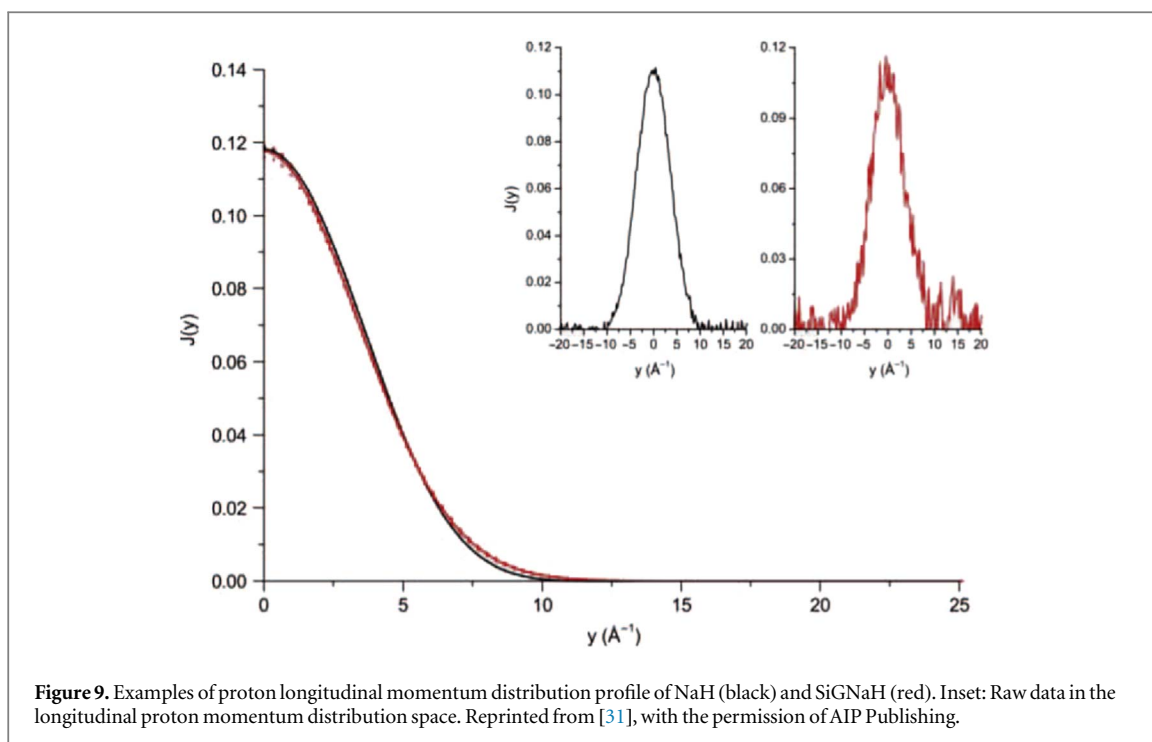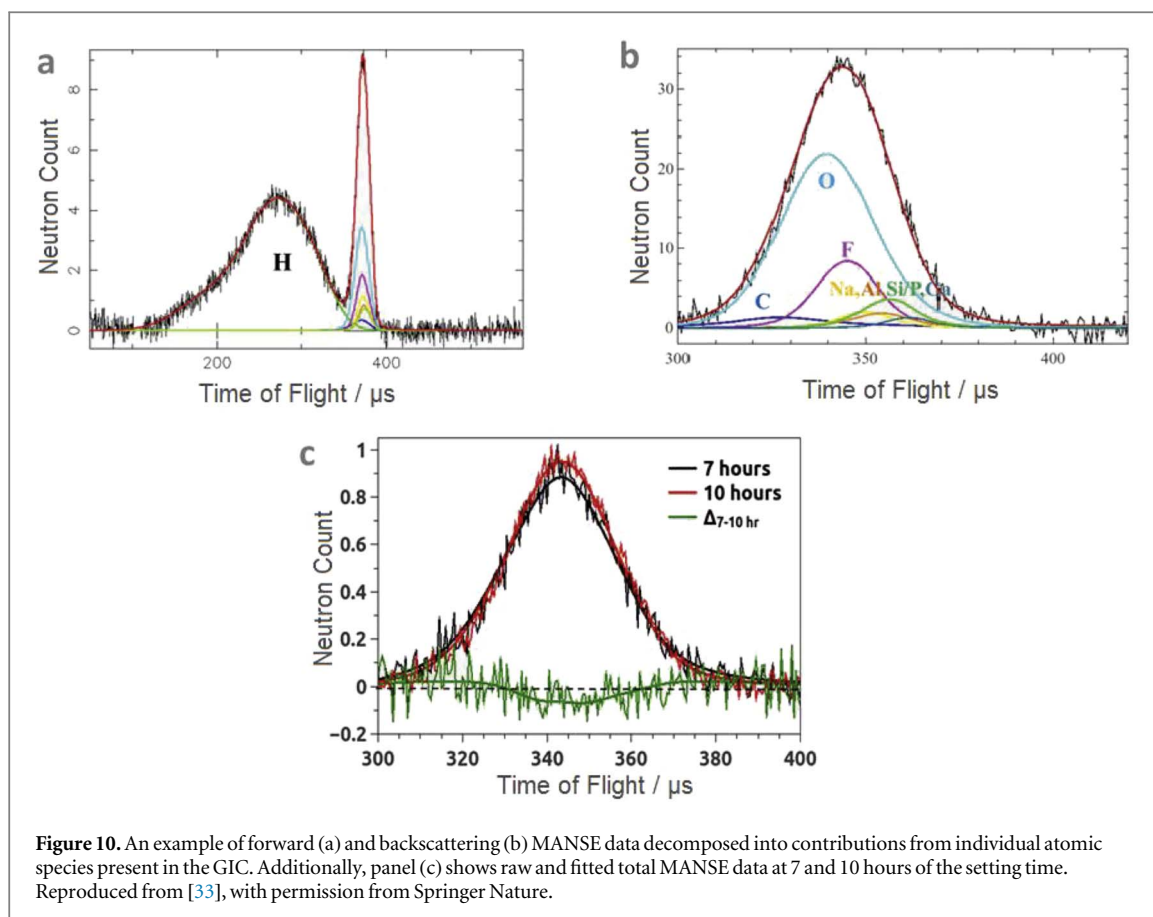
Figure 9. Examples of proton longitudinal momentum distribution profile of NaH (black) and SiGNaH (red). Inset: Raw data in the longitudinal proton momentum distribution space. Reprinted from [31], with the permission of AIP Publishing.

in figure 9 for the proton longitudinal momentum distribution. The experimental proton NMD shapes for NaH and SiGNaH are very similar, resulting in the values of the proton mean kinetic energy of ca. 69 meV. However, by making this comparison, one has to take into account the range of nanoparticle size distributions in SiGNaH, which may provide an effective means of inhomogeneous broadening of all momentum distributions. Thus, the underlying proton momentum distributions in SiGNaH are quite likely to be narrower than their counterparts in NaH, resulting in concomitant broadening of position distributions. Thus, protons in SiGNaH nanoparticles should be less localised than their counterparts in bulk NaH due to a smaller degree of binding (or confinement).

As atomic mass increases, the MANSE peak positions become closer and start overlapping. Thus, the task of peak isolation in MANSE spectra cannot be easily accomplished in the case of heavier nuclei. In such cases, the only way to provide a reliable MANSE data analysis protocol is to fix, in fitting the data, the ratios of the peak intensities, according to the known sample stoichiometry and tabulated total bound neutron scattering cross sections [3]. This technique works better in the backscattering regime due to larger peak separations of heavier masses. The technique of stoichiometric fixing, when applied to the MANSE data collected for SiGNaH nanoparticles in backscattering, provided some interesting results as far as the chemical environment of sodium ions is concerned. First of all, one observed a trend in which the width of the Na longitudinal momentum distribution systematically decreases when going from bulk NaH (the value of $7.2 \pm 0.4 \, \text{Å}^{-1}$), through SiGNaH (the value of $6.3 \pm 0.7 \, \text{Å}^{-1}$), to reach the lowest value of $5.3 \pm 0.2 \, \text{Å}^{-1}$ in the case of SiGNa [31]. Such a progression would normally indicate a decreasing degree of the confinement of the sodium ions. However, caution must be exercised when interpreting the data in such a way. Firstly, the higher value for the Na width in NaH is particularly important, as it indicates the increased potential felt by the Na nuclei in the ionic salt compared to the metallic state [31]. Moreover, the value for the Na profile width in SiGNaH is bracketed by those of NaH and SiGNa. However, it has to be borne in mind that the hydrogenation of the SiGNa precursor is usually not a perfect process and results in approximately only half of the available Na being reacted to give NaH, with the remaining still existing as amorphous Na in the gel [31]. Thus, the experimental value of the profile width in SiGNaH is rather reflecting this partial hydrogenation and should be interpreted as an average of the two environments [31]. In the case of the silicon, one observes similar NMD widths in both gel samples, which may reflect the unchanged Si tetrahedral coordination of the Si atoms in the SiO_4 units. As far as oxygen is concerned, the value of the width was $11.0 \pm 0.5 \, \text{Å}^{-1}$ in SiGNaH and $12.8 \pm 0.3 \, \text{Å}^{-1}$ in SiGNa, which was interpreted as the result of ionization of the amorphous Na at close contact with the O surface of the silica gel [31]. On the whole, the detailed shape analysis of the NMD of the proton and the application of the technique of stoichiometric fixing to MANSE data of all nuclei heavier than the proton resulted in a successful demonstration of the potential of the MANSE technique, as applied to the analysis of the degree of chemical binding and confinement of encapsulated nanoparticles in amorphous silica gel.

Figure 10. An example of forward (a) and backscattering (b) MANSE data decomposed into contributions from individual atomic species present in the GIC. Additionally, panel (c) shows raw and fitted total MANSE data at 7 and 10 hours of the setting time. Reproduced from [33], with permission from Springer Nature.

4.2. Bioactive glass-ionomer cements

Bioactive glass ionomer cement (GICs) have been in widespread use for the last forty years in dentistry and medicine. GICs are the product of a basic fluoro-phospho-alumino-silicate glass powder and an aqueous poly (acrylic) acid (PAA) solution. Although bio-compatible and caries-resistant, GICs remain too brittle for permanent implants. To this end, the MANSE study on GICs performed recently is a pioneering piece of research as it attempts to provide a non-destructive alternative to the otherwise material-damaging protocol of the assessment of the mechanical properties of these important materials [33]. Traditionally, damage tolerance has been assessed through two measures: (i) fracture toughness, K_c, and (ii) yield strength, σ_Y. A doubly logarithmic plot relating those two measures, referred to as the Ashby scheme, has been widely used to categorise conflicts between strength and toughness in composite materials [33]. GICs, similarly to other composite materials, place themselves in the lower left corner of the Ashby plot, exhibiting relatively low Yield strength and fracture toughness. Yet, they exhibit marked changes of K_c and σ_Y as a function of the setting time, as they are being transformed into rigid and inflexible cements [33]. Another mechanical measure, the compressibility κ relates directly to the shape of the interatomic potentials of a given system. The narrower and deeper the potential is, the stronger and more rigid the atomic cohesion. Moreover, more rigid materials have a higher shear modulus G and lower k. Most importantly, however, the correlation exists, whereby the product of G and k seems to be maximised for the most brittle materials, as opposed to the ductile ones [33].

These correlations, relating macroscopic mechanical properties to the microscopic world of the interaction potentials, together with the fact that MANSE nuclear quantum observables can be related to the shape of the local, effective potential surface experienced by the nuclei in a given material, have become the source of inspiration for the basic idea behind the MANSE experiment on GICs [33]. Operationally, the idea boiled down to performing an experiment in which MANSE observables would be monitored as a function of time during the setting process for non-destructive monitoring of the mechanical toughness K_c and cohesion on the atomic level. Figure 10 shows an example of forward (a) and backscattering (b) MANSE data decomposed into contributions from individual atomic species present in the GIC. Additionally, panel (c) in this figure shows raw and fitted total MANSE data at 7 and 10 hours of the setting time.

The basic result of the application of MANSE to monitor the GIC setting process was that the temporal evolution of NMD widths, both for individual atomic species and averaged over the GIC stoichiometry, was found to be markedly non-monotonic [33]. Three distinct regions in the setting time corresponding to three different types of behaviour were identified: (i) the so-called glass-ionomer coupling point (CP), (ii) the initial
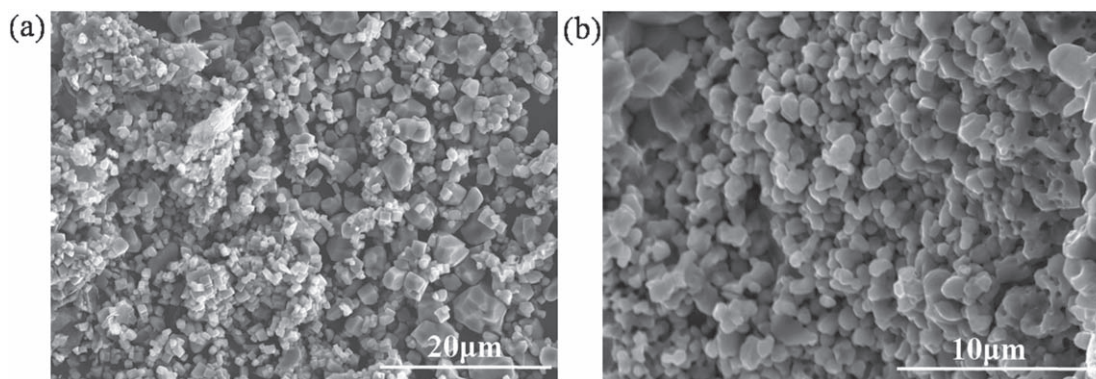
Figure 11. The morphology of prepared TiC particles in the Cu-4Ti-C composite. See text for details. Reprinted from [43], Copyright (2018), with permission from Elsevier.

setting point (ISP), and (iii) the interfacial stress zone (ISZ). CP was defined as an early setting point where material toughness unexpectedly recovered. ISP was defined as a clear maximum, at ca 8 hours of the setting time, where the atomic cohesion is greatest, and ISZ as a point, at ca. 15 hours of the setting time, where atomic cohesion momentarily dropped before recovering [33]. On the whole, MANSE was found to be a potent tool for the investigation of atomic cohesion, following a rule of thumb stating that when the NMD widths were lower, average atomic cohesion was also found to be lower, interatomic potentials shallower and wider and thus the material tougher [33]. Moreover, upward shifts in temperature with time for the features CP, ISP and ISZ were observed as the setting temperature increased. Finally, when averaged over the GIC stoichiometry, the NMD widths were also found to correlate well with the inverse of fracture toughness across a range of related materials [33].
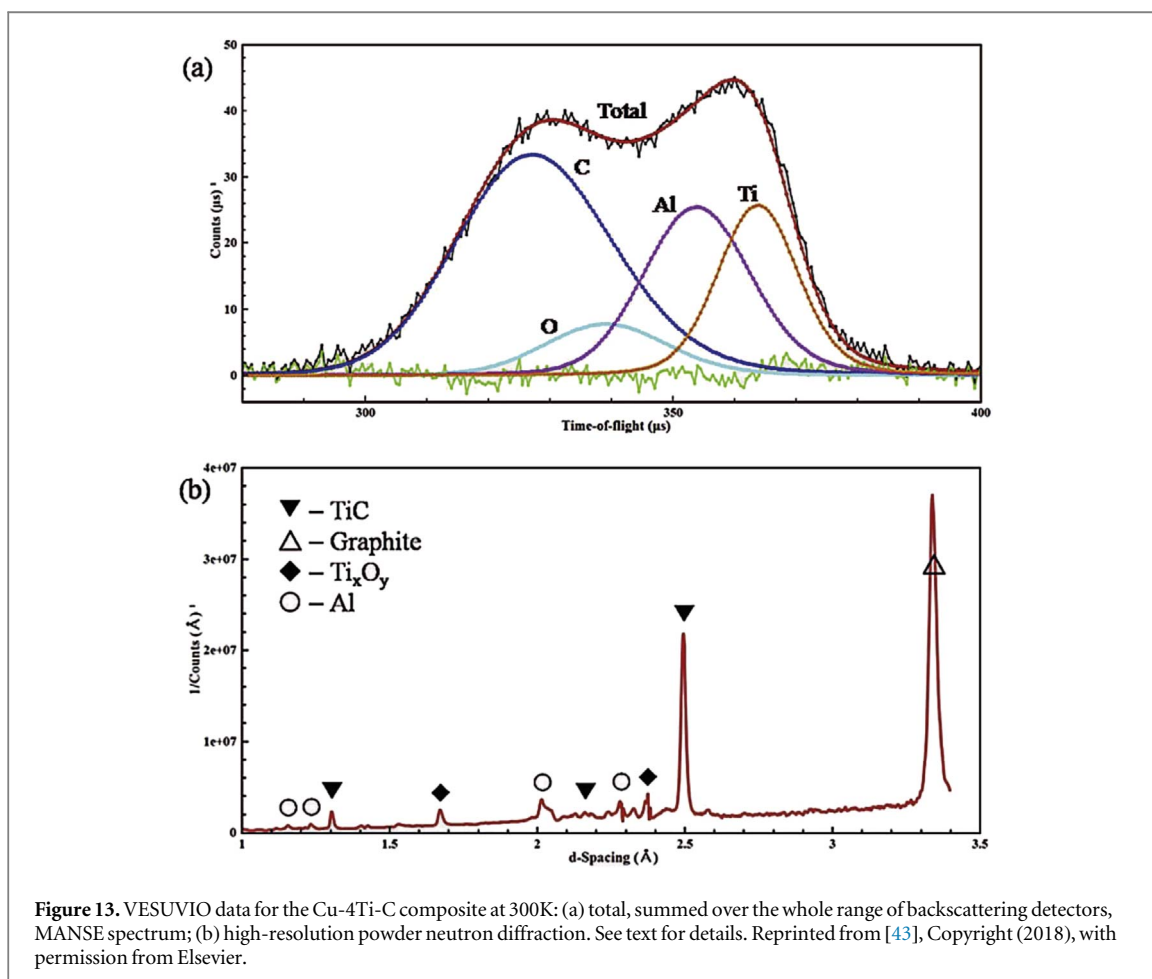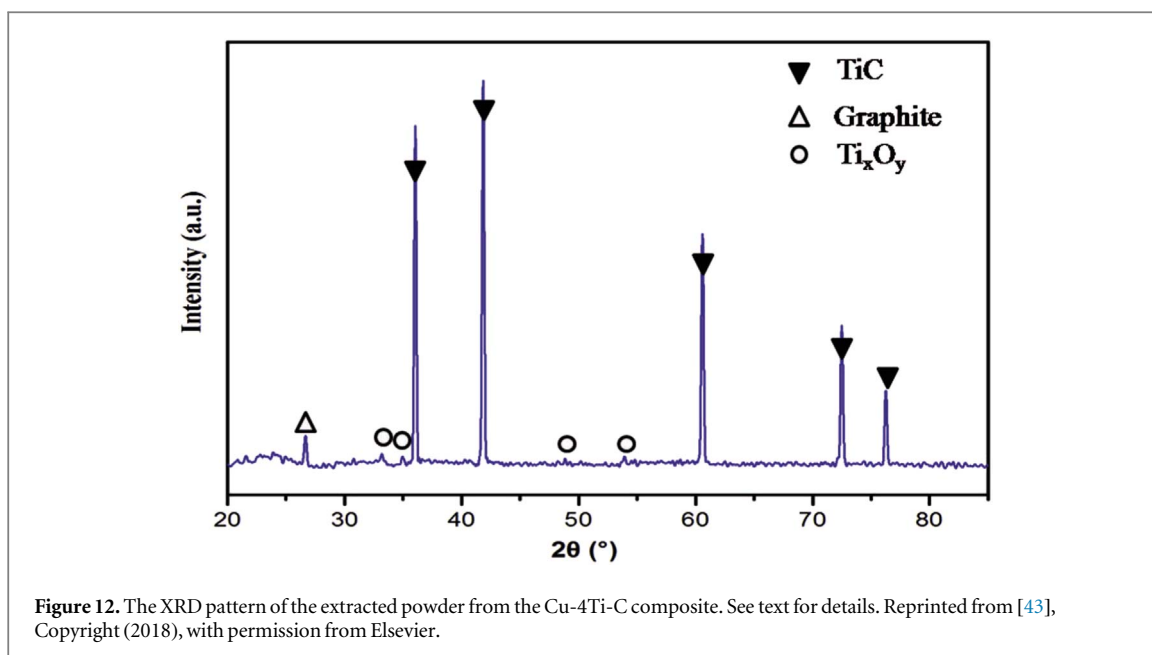
4.3. TiC-reinforced Cu-Ti-C composites

Copper matrix composites, where copper is reinforced by ceramic materials such as SiC, Al_2O_3 and Ti_2O_3, exhibit both excellent mechanical and electrical properties [34–39]. Among them, titanium carbide (TiC), due to its excellent properties such as high stiffness, hardness and melting point, has drawn a lot of attention recently [40, 41]. Importantly, it has been observed that the addition of TiC deteriorates the electrical and thermal conductivities of the resultant composite to a much lesser extent than is the case for other copper composites [42].
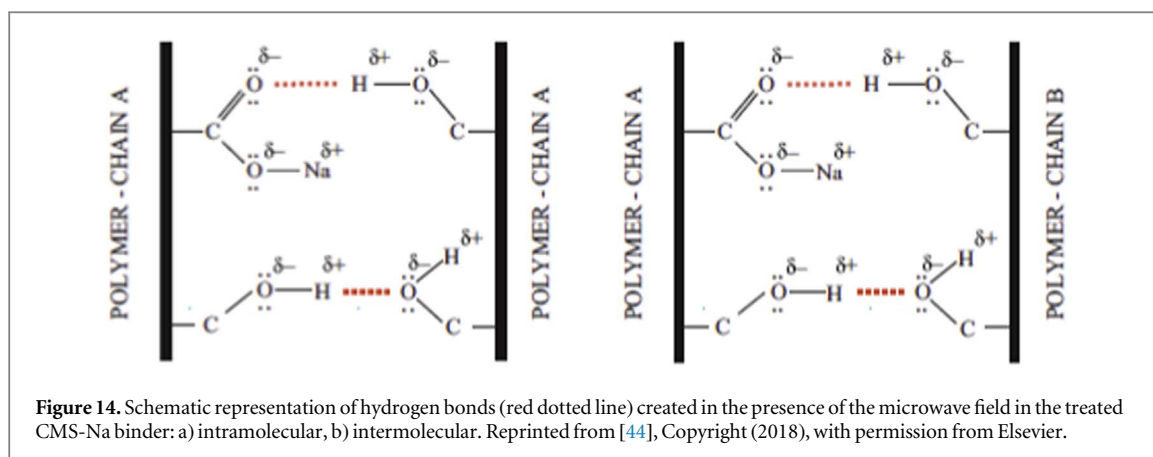
MANSE was employed on VESUVIO, along with scanning electron microscopy (SEM) equipped for energy-dispersive x-ray spectroscopy (EDS) and x-ray diffraction (XRD), to study the Cu-Ti-C composites [43]. The Cu-Ti-C composites with the nominal chemical composition of Cu 4 wt.% Ti 1 wt.% C (hereinafter referred to as Cu-4Ti-C), corresponding to 1:1 molar ratio of Ti and C, were produced by *in-situ* synthesis of TiC in Cu melts. As for the sample structure and morphology, the SEM and XRD results confirmed that a newly formed particle-like phase forms in the Cu matrix with most TiC particles ranging from 0.5 to 2 μm, while a few of them are larger than 3 μm. The distribution of TiC is relatively uniform in the matrix as a whole. However, locally, TiC tends to form agglomerations, especially the larger TiC particles (see figure 11) [43].

However, XRD results of the extracted powder show besides diffraction peaks of TiC, peaks of the graphite and Ti_xO_y (figure 12). This suggests that not all graphite added in the synthesis reacted with soluble Ti to form TiC, thus inevitably leading to the residual of Ti. Moreover, the results of the EDS analysis indicate that there is a certain amount of Ti dissolved into Cu matrix [43]. These XRD and EDS result provide the first important clues as to the sample stoichiometry, a tantamount to successful MANSE analysis. To this end, further clues are provided by the results of the XRD analysis. Based on the XRD results, the lattice parameter of 4.327 79 Åwas found, which, using the Storms formula, yielded the TiC stoichiometric composition of $TiC_{0.9}$ [43]. Assuming that the average composition of Ti in the matrix is 0.798 wt.%, according to the EDS results, and that all the other Ti reacted with graphite to form $TiC_{0.9}$, it was evaluated that only about 72% of graphite reacted with Ti to form TiC. Given that some Ti has reacted with O to form Ti_xO_y, as the XRD analysis shows (see figure 12), it is impossible for all the residual graphite to remain in the composite and the actual amount of graphite involved in the reaction would be less than 72% [43].

The results of the XRD analysis were confirmed by the high-resolution neutron diffraction on VESUVIO, as shown in panel (b) in figure 13 Neutron diffraction, being more sensitive and accurate in detecting light elements such as C, corroborated the results of the elemental analysis provided by the XRD.

Figure 12. The XRD pattern of the extracted powder from the Cu-4Ti-C composite. See text for details. Reprinted from [43], Copyright (2018), with permission from Elsevier.

Figure 13. VESUVIO data for the Cu-4Ti-C composite at 300K: (a) total, summed over the whole range of backscattering detectors, MANSE spectrum; (b) high-resolution powder neutron diffraction. See text for details. Reprinted from [43], Copyright (2018), with permission from Elsevier.

In panel (a) in figure 13, the MANSE response functions appear at increasing TOF values for isotopes with increasing atomic mass. One can clearly distinguish peaks of Al, C, O, and Ti, with the Al peak coming from the sample container used on the VESUVIO beam line. For the analysis of the MANSE results, simple Gaussian profiles were assumed for all elemental response functions. The fitting of MANSE data yielded 12.9 ± 0.3; 11.3 ± 0.4; and 14.2 ± 0.7 Å^{-1}, for C, O, and Ti, respectively. In the case of Ti, the fitting result was 20% lower than the Debye model predictions for pure titanium at 300K. Thus, the degree of binding of titanium in the

Figure 14. Schematic representation of hydrogen bonds (red dotted line) created in the presence of the microwave field in the treated CMS-Na binder: a) intramolecular, b) intermolecular. Reprinted from [44], Copyright (2018), with permission from Elsevier.
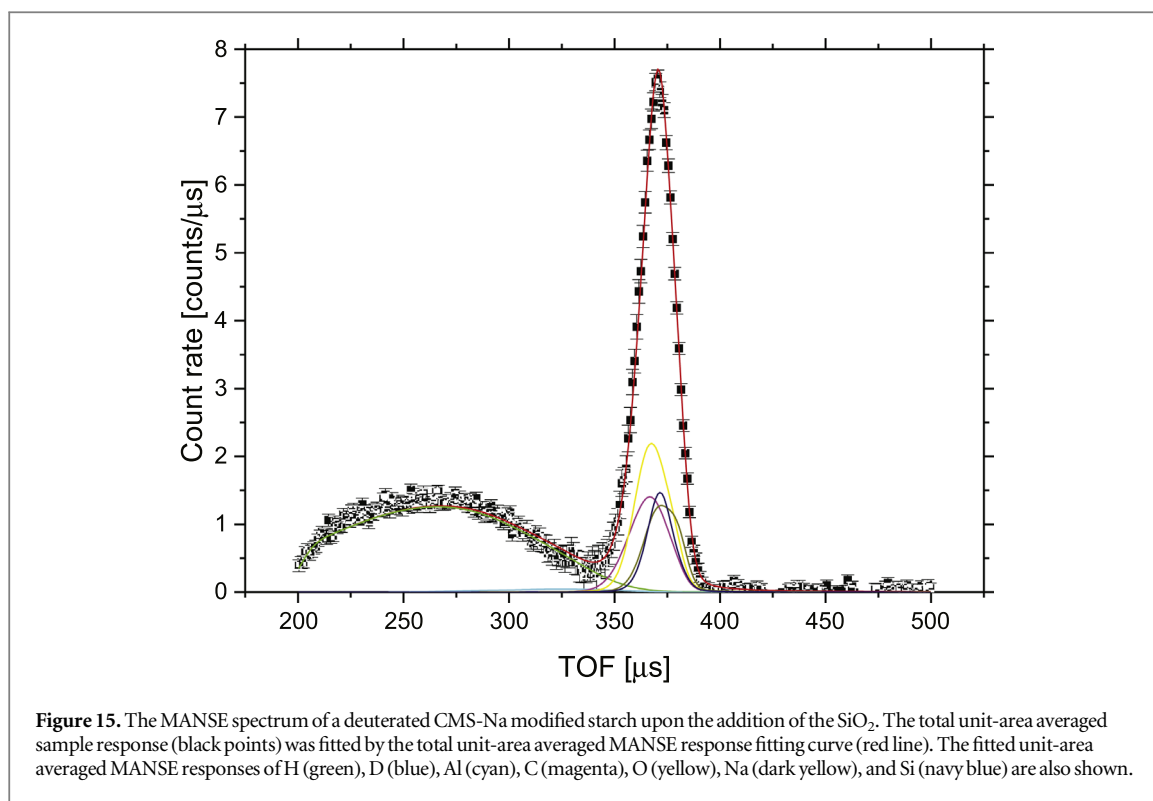
Cu-4Ti-C composite, when averaged over all binding sites, is lower than in pure polycrystalline Ti, also possibly due to the incomplete reaction of graphite and Ti. Importantly, the technique of stoichiometric fixing was not employed during the MANSE data analysis in order to extract, from the relative (expressed in the units of the total) MANSE peak intensities, the value of the C/Ti molar ratio. The obtained value was 1.28 ± 0.05, thus further confirming that some Ti has been left in the Cu matrix, which is etched off during extraction of the powder.

Taken together, the results of the MANSE and diffraction experiments confirm the existence of Ti and C residues in the Cu-4Ti-C composites. However, because of the relatively good electrical conductivity of graphite, the proposed route of *in-situ* synthesis is still acceptable, as it still yields composites of relatively high electrical conductivity. Moreover, it was proposed that, in order to further improve the electrical properties of the composites, boron can be added. Boron, when dissolved in the solid matrix, will bind titanium, thus forming TiB_2, thus leading to the overall improvement of the electric properties of the materials.

4.4. Structure of binders based on sodium carboxymethyl starch

One of the most recent examples of MANSE work on nanocomposite materials is the investigation of the hardening process of moulding sands on quartz matrices bound by polymer binders containing carboxyl and hydroxyl groups. Natural polymers, and amongst them polysaccharides (including starch), have been used extensively as foundry adhesives. Starch would have been an almost ideal binder if it were not for the fact that it is insoluble in cold water. Hence, the use of modified cold-water-soluble starch is an interesting, cost-effective alternative. One of the forms that have recently attracted a lot of attention is the starch modified by carboxymethylation to sodium carboxymethyl starch (hereinafter referred to as CMS-Na), with hydroxyl groups substituted by the –COONa groups in the anhydroglucose unit (AGU) [44]. Apart from the chemical structure modification, 'curing' is often employed in industrial processing, whereby conventional heating and/or chemical reaction leads to physically or chemically cross-linked structures exhibiting mechanical properties almost tailored for mould and casting. Conventional thermal treatment of modified starches, however, is a high-energy and time-consuming process. This has motivated the application of microwave radiation as a curing agent, leading to much shorter processing and more efficient industrial processing protocols. After purely chemical engineering work, spectroscopic studies of structure-related properties followed in the literature. One of the pioneering studies consisted of a set of spectroscopic measurements (FTIR, FTRaman, XRD) carried out for CMS-Na starches characterised by different numbers of substituent groups (–CH$_2$COONa) attached at the AGU, referred to as the substitution ratio, DS [44]. The red shift and change in intensity of the band, ranging from 3000 to 3800cm^{-1}, associated with the hydrogen bonds in the hydroxyl groups, was observed as a function of DS before the exposure to microwaves. Such changes can be interpreted as a growing content of polarizable bonds. This important observation leads to the assumption that, during the treatment of moulding sands with water-soluble binders in the microwave field, the high-DS CMS-Na starch samples should absorb the microwave radiation to a greater extent. These changes are attributed to the formation of a network of new inter- and intramolecular hydrogen bonds after solvent (water) evaporation.

From a detailed analysis of the IR and Raman spectra, a multi-step mechanism was proposed that describes the radiation-induced formation of a hydrogen-bond network (physical cross-linking, see figure 14). In the first step, microwave radiation supplies to the system the energy portion, which shifts partial charges (present in functional groups of hydrophilic polymers), leading to the so-called dipole polarisation, which is sufficient for rotations of polymer granules. In consequence, the energy distribution leads to the activation of polar groups and the formation of new bonds. The resonance stabilisation of the carboxylic group is disturbed in the

Figure 15. The MANSE spectrum of a deuterated CMS-Na modified starch upon the addition of the SiO$_2$. The total unit-area averaged sample response (black points) was fitted by the total unit-area averaged MANSE response fitting curve (red line). The fitted unit-area averaged MANSE responses of H (green), D (blue), Al (cyan), C (magenta), O (yellow), Na (dark yellow), and Si (navy blue) are also shown.

microwave field. As a result, the hydroxylic fragment of this group is more likely to split off. That is why—under the influence of microwave radiation—the cross-linking reaction of neighbouring polymer chains occurs by means of dehydration (by anhydride bonds). It is then the additionally formed hydrogen bonds that determine the binding properties of moulding sands with CMS-Na binders. Moreover, the ability to form hydrogen bonds also depends on the degree of the substitution, DS, with the higher DS value samples being much more prone to creating a bigger number of hydrogen bonds. Interestingly, as evidenced by the results of the XRD data analysis in the starch samples, the newly formed hydrogen bond network did not lead to the formation of ordered crystalline structures with all microwave-treated starch samples remaining highly amorphous [44].

The fact that according to the combined FTIR, FTRaman and XRD study, CMS-Na modified and microwave-irradiated starch shows the shifts of the pVDoS of hydrogen to higher frequencies constituted the main source of motivation for the newly proposed MANSE study. MANSE, measuring the variance of momentum distributions being proportional to the first moment of the atom–projected VDoS, can be very sensitive to shifts of vibrational bands induced by the cross-linking process. MANSE has been applied to CMS-Na modified starch and CMS-Na modified starch mixed with the SiO$_2$ matrix to investigate the changes in binding and ordering of hydrogen bonds in the CMS-Na modified starch upon the addition of the SiO$_2$, with both samples treated with microwave radiation. As the microwave radiation produces a network of hydrogen bonds that contains polar binder groups (−OH) and silane groups of the mineral matrix surface layer (Si-OH), the anticipated MANSE response of the protons in the system contains, in principle, a site-averaged mixture of elemental responses due to momentum distributions of protons in both polar binder and silane groups. Thus, in order to render the MANSE technique site- rather than mass-selective, Si-OH groups, present on the surface of mineral SiO$_2$ matrix, and OH groups, present in the etherified starch sodium, were deuterated by immersing samples in heavy water prior to MANSE experiments.

The MANSE spectrum of the CMS-Na modified starch in the mineral SiO$_2$ matrix is shown in figure 15 with the total response as well as the responses of other constituent masses fitted using the CAAD technique.

The CAAD fit resulted in well-resolved spectral responses of H, D, C, O, Na, and Si nuclei. The presence of the response spectra of both H and D was interpreted as the result of non-perfect deuteration, whereby the hydrogen response resulted from not exchanged -OH groups. Conversely, the deuterium response resulted from the -OD groups, as well as the residual heavy water, still present in the sample (probably in a tightly bound form). The NMDs of all constituent nuclei were assumed to be of purely Gaussian form. The values of the fitted widths of the NMDs obtained from the CAAD fit were 4.71 ± 0.03, 5.70 ± 0.04, 11.6 ± 0.1, 11.3 ± 0.1, 15.7 ± 0.1, and 17.6 ± 0.1 Å^{-1}, for H, D, C, O, Na, and Si nuclei, respectively. The same model was applied to the deuterated CMS-Na modified starch sample without the SiO$_2$ matrix. The obtained values of the NMD widths were 4.89 ± 0.03, 5.78 ± 0.04, 11.9 ± 0.1, 11.8 ± 0.1 and 16.9 ± 0.1 Å^{-1}, for H, D, C, O, Na, and Si nuclei,

respectively. These values are systematically higher than their counterparts for the sample containing the SiO_2 matrix. Higher values of NMD widths at the same temperature of an NCS experiment signify tighter binding (and thus higher values of force constants). Moreover, high-resolution neutron diffraction, performed concurrently on both samples on VESUVIO, confirmed the previous XRD results, pointing out a lack of long-range order in the sample and their amorphous character. In light of both types of results, the most natural interpretation is that the introduction of the mineral matrix causes disruption, disordering and weakening of the hydrogen bond network, whereby the proportion of broken, bent and distorted bonds increases compared to the sample without the matrix. This result provides an important starting point for further comparison of neutron responses of samples prior to and after the microwave radiation treatment. Operationally, the MANSE analysis also continues to demonstrate to be a potent tool for non-destructive elemental analysis, so important in the case of the comparison of deuterated and native variants of otherwise similar chemical systems.

5. Summary and outlook

Owing to the methodological advances at the VESUVIO beamline at ISIS Neutron and Muon Source, STFC Rutherford Appleton Laboratory, material characterisation by concurrently employing mass-selective neutron Compton spectroscopy, high-resolution neutron diffraction and neutron transmission and γ–Dopplerimetry has become possible [2–4, 23]. This unique combination of neutron techniques not only enables streamlined, more robust experimental protocols but also creates hitherto unprecedented synergies. Simultaneous characterisation of sample composition, degree of crystallinity, and assessment of all necessary spectroscopic data correction procedures is one of them. The ability to use the γ–Dopplerimetry to infer information about the local chemical dynamics of heavy atomic species despite the fact that the total neutron Compton response of the same sample contains overlapping peaks of heavy and lightweight atomic species is the other. Moreover, when augmented with modern material modelling techniques, such concurrent neutron measurements enable global benchmarking of experimental results against the same underlying structural and dynamical models over an unprecedented range of spatiotemporal scales.

Tapping into this unique potential of combined experimental and modelling methodologies, in recent years, the VESUVIO beamline has witnessed an unprecedented upsurge of activity as far as nanocomposite material characterisation is concerned. In this review, a few examples of such studies have been described, including encapsulated nanoparticles in amorphous silica gel, bioactive glass-ionomer cement, Cu-Ti-C composites, and sodium carboxymethyl starch-based binders in the presence of a mineral matrix. The concurrent characterisation of the average structure and local dynamics of individual atomic species in these systems has been possible not only owing to advances in instrumentation and data treatment methodology but -crucially— due to novel material modelling protocols that rely on robust approximations.

Despite the undisputed success of the broadband and mass-selective neutron material characterisation techniques, a few challenges still lie ahead. Perhaps the most important one is related to the experimental turnover of individual neutron beamlines at large-scale facilities like ISIS. Optimised, streamlined, and robust experimental protocols employing versatile sample environments are necessary. However, and perhaps most importantly, one needs efficient material modelling protocols. This latter goal is especially challenging when trying to account for nuclear quantum effects in disordered composite systems. To this end, recent advances in the efficient path integral molecular dynamics simulation schemes involving classical force fields are perhaps the most promising. Moreover, machine learning-augmented molecular dynamics can provide an alternative avenue for robust and efficient composite material modelling.

Data availability statement

All data that support the findings of this study are included within the article (and any supplementary files).

ORCID iDs

Matthew Krzystyniak ⓘ https://orcid.org/0000-0003-0307-6871

References

[1] Andreani C, Colognesi D, Mayers J, Reiter G and Senesi R 2005 *Adv. Phys.* **55** 377
[2] Andreani C, Senesi R, Krzystyniak M, Romanelli G and Fernandez-Alonso F 2015 Atomic quantum dynamics in materials research *Neutron Scattering–Applications in Biology, Chemistry, and Materials Science* ed F Fernandez-Alonso and D L Price (Academic Press) p 403

[3] Andreani C, Krzystyniak M, Romanelli G, Senesi R and Fernandez-Alonso F 2017 *Adv. Phys.* **66** 1
[4] Andreani C, Senesi R, Krzystyniak M, Romanelli G and Fernandez-Alonso F 2018 *La Rivista del Nuovo Cimento* **41** 291
[5] Mayers J and Reiter G 2012 *Meas. Sci. Technol.* **23** 045902
[6] Pietropaolo A and Senesi R 2011 *Phys. Rep.* **508** 45
[7] Romanelli G *et al* 2017 *Meas. Sci. Technol.* **28** 095501
[8] Krzystyniak M and Fernandez-Alonso F 2011 *Phys. Rev.* B **83** 134305
[9] Krzystyniak M, Romanelli G and Fernandez-Alonso F 2019 *Analyst* **144** 3936–41
[10] Krzystyniak M, Gutmann M J, Romanelli G, Trenikhina Y, Romanenko A and Fernandez-Alonso F 2018 *J. Phys. Conf. Ser.* **1055** 012006
[11] Dorner B 2006 *Nucl. Instrum. Methods Phys. Res., Sect.* B **247** 390–6
[12] Lalik E, Parker S F, Irvine G, da Silva I, Gutmann M J, Romanelli G, Drużbicki K, Kosydar R and Krzystyniak M 2023 *Energies* **16** 5496
[13] Senesi R, Kolesnikov A I and Andreani C 2014 *J. Phys. Conf. Ser.* **571** 012007
[14] Prisk T R, Kolesnikov A I, Granroth G E, Lin J L and Heuser B J 2020 *J. Alloys Compd.* **818** 152832
[15] Dawidowski J, Granada J R, Santisteban J R, Cantargi F and Rodríguez Palomino R A 2013 Appendix—neutron scattering lengths and cross sections *Neutron Scattering—Fundamentals* ed F Fernandez-Alonso and D L Price (Academic Press) p 471
[16] Mayers J, Fielding A and Senesi R 2002 *Nucl. Instrum. Methods Phys. Res., Sect.* A **481** 454–63
[17] Dawidowski J, Blostein J J and Granada J R 2006 *J. Instrum.* **1** P06002
[18] Romanelli G, Krzystyniak M and Fernandez-Alonso F 2018 *J. Phys. Conf. Ser.* **1055** 012015
[19] Krzystyniak M *et al* 2018 *J. Phys. Conf. Ser.* **1021** 012026
[20] Krzystyniak M *et al* 2018 *J. Phys. Conf. Ser.* **1055** 012004
[21] Krzystyniak M, Seel A G, Richards S E, Gutmann M J and Fernandez-Alonso F 2014 *J. Phys. Conf. Ser.* **571** 012002
[22] Mayers J 2010 *Meas. Sci. Technol.* **22** 015903
[23] Price D L and Fernandez-Alonso F 2013 Ch 1—an introduction to neutron scattering *Neutron Scattering—Fundamentals* ed F Fernandez-Alonso and D L Price (Academic Press) p 1
[24] Ceriotti M *et al* 2016 *Chem. Rev.* **116** 7529
[25] Cazorla C and Boronat J 2017 *Rev. Mod. Phys.* **89** 035003
[26] Markland T E and Ceriotti M 2018 *Nature Reviews Chemistry* **2** 0109
[27] Zielinski T J, Harvey E, Sweeney R and Hanson D M 2005 *J. Chem. Educ.* **82** 1880
[28] Lévy M 1950 *Proceedings of the Royal Society of London. Series A, Mathematical and Physical Sciences* **204** 145–69
[29] Parmentier A, Andreani C, Romanelli G, Shephard J J, Salzmann C G and Senesi R 2017 *Frontiers of Physics* **13** 136101
[30] Krzystyniak M, Drużbicki K and Fernandez-Alonso F 2015 *Phys. Chem. Chem. Phys.* **17** 31287
[31] Seel A G, Sartbaeva A, Mayers J, Ramirez-Cuesta A J and Edwards P P 2011 *J. Chem. Phys.* **134** 114511
[32] Sartbaeva A *et al* 2010 *J. Cluster Sci.* **21** 543
[33] Tian K V *et al* 2015 *Nat. Commun.* **6** 8631
[34] Cheng B *et al* 2017 *J. Alloys Compd.* **722** 852
[35] Hu Z Y, Liu J X, Li S K, Wang Y C, Guo W Q and Ma S M 2017 *Mater. Sci. Eng.* A **708** 43
[36] Arnaud C *et al* 2016 *Carbon* **96** 212
[37] Guo M, Shen K and Wang M 2009 *Acta Mater.* **57** 4568
[38] Zhou Y and Hu M 2017 *Comput. Mater. Sci.* **129** 129
[39] Qin P, Ge Z H and Feng J 2017 *J. Alloys Compd.* **696** 782
[40] Song Q, Xu Q, Xu L, Ning Z, Lou T, Xie H, Qi Y and Yu K 2017 *J. Alloys Compd.* **690** 116
[41] Yu H *et al* 2017 *J. Alloys Compd.* **701** 244
[42] Rathod S *et al* 2009 *Materials Science and Engineering:* A **502** 91
[43] Ding H, Liu Q, Wang X, Fan X and Krzystyniak M 2018 *J. Alloys Compd.* **766** 66
[44] Kaczmarska K *et al* 2018 *Spectrochim. Acta, Part* A **199** 387–93